CFD ANALYSES FOR ADVANCED PUMP DESIGN

F.J. de Jong, S-K. Choi, and T.R. Govindan

Scientific Research Associates, Inc.
Glastonbury, CT 06033

April 1994

Final Report R94-9081-F

Prepared Under

Contract NAS8-38866

for

National Aeronautics and Space Administration
George C. Marshall Space Flight Center

TABLE OF CONTENTS

LIST OF FIGURES

1. INTRODUCTION

State-of-the-art in pump design for space shuttle, space transport, or general ETO propulsion systems currently is a combination of experience, simple analyses with empiricism to estimate overall performance, and input from a database generated by experiments. This aspect of the design process will remain largely unchanged in the near future, due to the fact that current CFD viscous flow codes are "analysis" codes, rather than "inverse design" codes; i.e., they analyze the flow for a specified geometry and inflow conditions, rather than determine the geometry required to provide a desired flow field. With this limitation, CFD can be best utilized in modern pump design by first producing a "baseline" design produced by current design practice and utilizing state-of-the-art CFD codes to change design details so as to evolve the base design to an improved, advanced, and hopefully near-optimum design with improved performance. This process would utilize the insight which the computations provide into the flow field structure, to refine the baseline design or suggest new geometric configurations to achieve desired performance.

Analysis and/or design of centrifugal turbomachinery, as is represented by impellers, pumps and inducers, presents a considerably more difficult challenge than their axial counterparts. In axial turbomachinery, two-dimensional inviscid analysis can provide valuable information for blade section behavior, and this analysis does provide valuable information, as long as the flow is close enough to design so that flow separation is absent or minimal. However, in the case of centrifugal machinery, where the blade-to-blade and hub-to-shroud distances are small compared to the passage length, viscous effects are accentuated over the entire passage flow field. Furthermore, the strong passage curvature, combined with the passage rotation, leads to generation of strong secondary flows. The result of these characteristics is that a CFD approach requires a full three-dimensional Navier-Stokes analysis.

In the work discussed here, a state-of-the-art three-dimensional Navier-Stokes code was used for design analysis of the STME impeller, one of the tasks of the NASA/MSFC Pump Stage Technology Team (Refs. 1-4). The STME baseline impeller flow field was simulated and, based upon the simulation described here and simulations performed by other members of the NASA/MSFC Pump Stage Technology Team, an advanced, "optimized" design was developed which, in turn, was analyzed. Prior to this application the code was assessed through comparison of its results with experimental data from a Rocketdyne inducer. In addition, a simulation was made for the SSME HPFTP impeller.

The present report describes the CFD code used for these simulations, as well as results obtained. Further results, including comparison of the results of this simulation with results obtained by other investigators, are given by Garcia et al. (Refs. 2-5).

2. ANALYSIS

2.1 Navier-Stokes Equations

Solution of the flow field, both in the centrifugal impellers and in the inducer, was obtained from a solution of the Reynolds-averaged, compressible Navier-Stokes equations. The governing equations were expressed in a rotating cylindrical coordinate system fixed to the inducer or impeller axis. In this coordinate system the mass, momentum, and energy conservation equations are:

$$\frac{\partial \rho}{\partial t} + \nabla \bullet (\rho \mathbf{U}) = 0 \tag{1}$$

$$\frac{\partial (\rho \mathbf{U})}{\partial t} + \nabla \bullet (\rho \mathbf{U}\mathbf{U}) + 2\rho\omega x \mathbf{U} + \rho\omega x \omega x \mathbf{r} = -\nabla p + \nabla \bullet \vec{\tau} \tag{2}$$

$$\frac{\partial (\rho h)}{\partial t} + \nabla \bullet (\rho \mathbf{U} h) = \frac{Dp}{Dt} - \nabla \bullet \mathbf{q} + \Phi \tag{3}$$

where **U** is the velocity vector in the rotating frame of reference, ω is the rotation vector, and **r** is a vector from the axis of rotation to the point under consideration.

The stress tensor (molecular and turbulent) $\vec{\tau}$ is given by

$$\tau_{ij} = 2\mu_{eff} e_{ij} - 2/3 \mu_{eff} \nabla \bullet \mathbf{U} \delta_{ij} \tag{4}$$

where the rate of the strain e_{ij} is given by

$$e_{ij} = 1/2 \left[\frac{\partial u_i}{\partial x_j} + \frac{\partial u_j}{\partial x_i} \right] \tag{5}$$

and where the effective viscosity μ_{eff} is the sum of the molecular and turbulent viscosities

$$\mu_{eff} = \mu + \mu_T \tag{6}$$

Here the turbulent viscosity μ_T is obtained from the turbulence model. Φ is the viscous dissipation per unit volume, which can be expressed as

$$\Phi = \mu_{eff}\left[2e_{ij}e_{ij} - 2/3(\nabla \bullet \mathbf{U})^2\right] \tag{7}$$

while the heat flux vector **q** is given by

$$\mathbf{q} = -(\kappa + \kappa_T)\nabla T \tag{8}$$

Here κ and κ_T are molecular and turbulent thermal conductivities, respectively. In the present analysis, κ and κ_T are obtained assuming constant molecular and turbulent Prandtl number Pr and Pr_T, i.e.,

$$\kappa = \frac{\mu c_p}{\mathrm{Pr}} \tag{9a}$$

$$\kappa_T = \frac{\mu_T c_p}{\mathrm{Pr}_T} \tag{9b}$$

A simple mixing-length type eddy viscosity model was used in the inducer/impeller computations, in which a mixing length distribution is specified normalized by a local freestream mixing length and modified to account for near-wall damping. The local freestream mixing length is proportional to a local shear layer thickness, which can be computed from the solution, or, as was done in the present calculations, can be specified. All boundary layers were assumed to be turbulent.

2.2 Numerical Solution Procedure

A general non-orthogonal coordinate transformation to a body-fitted grid is used to handle complex geometries in the solution procedure. The governing equations are solved by a Linearized Block Implicit (LBI) scheme (Refs. 6-7).

The method can be outlined as follows: the governing equations are replaced by an implicit time difference approximation, optionally a backward difference or Crank-Nicholson scheme (a backward time-difference scheme was used in the present application). Terms involving nonlinearities at the implicit time level are linearized by Taylor series expansion about the solution at the known time level, and spatial difference approximations are introduced. The result is a system of multidimensional coupled (but linear) difference equations for the dependent variables at the unknown or implicit time level. To solve these difference equations, the Douglas-Gunn procedure for generating alternating-direction implicit (ADI) splitting schemes is introduced in its

natural extension to systems of partial differential equations. This ADI splitting technique leads to systems of coupled linear difference equations having narrow block-banded matrix structures which can be solved efficiently by standard block-elimination methods. Details are given in Refs. 6-7.

In the present application, three-point central differences are used in the transformed coordinate system, and artificial dissipation terms of the form

$$\frac{\partial}{\partial x_j}\left[(\mu_{art})_j \frac{\partial \phi}{\partial x_j}\right] \tag{10}$$

are added to the governing equations for each coordinate direction j. The variable ϕ corresponds to the velocity component U_i for the x_i-direction momentum equation, the density ρ for the continuity equation, and the enthalpy h for the energy equation. The coefficient $(\mu_{art})_j$ is obtained from the relation

$$\rho U_j \Delta x_j \leq (1/\sigma_d)\left[\bar{\mu}+(\mu_{art})_j\right] \tag{11}$$

where Δx_j is the grid spacing at the point in question, while $\bar{\mu}$ corresponds to the effective viscosity μ_{eff} for the momentm equation, μ_{eff}/Pr for the energy equation, and is zero for the continuity equation. The artificial dissipation coefficient σ_d lies between 0 (no dissipation) and 0.5 (full artificial dissipation).

2.3 Grid Generation

An important component in a three-dimensional Navier-Stokes simulation is grid generation. Grid generation for the present study was accomplished by a variant of the algebraic procedure of Govindan, et al. (Ref. 8), originally developed for centrifugal impellers. Modifications were included to allow nonzero blade thickness, splitter blades, and hub/shroud cavities upstream or downstream of the (main) blades. A brief description of this generalized procedure is given below.

The overall procedure consists of two parts: the geometry definition and the actual grid generation. In the geometry definition part of the procedure, data is read that describes the blade surfaces and, if available, the hub and shroud surfaces. First, this data is converted to a cylindrical coordinate system (if it is not already given in this form). Let these coordinates be denoted by r, θ, z, where z is the axial coordinate (along the impeller or inducer axis). A series of spline fits is then constructed to define the geometry: on each blade surface, r, θ, and z are spline-fit as a function of

arc length along streamwise-like lines in the r-z plane. Upstream and downstream blade extensions are defined such that they are aligned with the blade camber surface at the leading and trailing edge. These extensions are nominally helical upstream of the blade, and either helical (for inducers) or radial (for impellers) downstream. After the geometry has been defined, a grid is generated in the r-z plane: grid point distributions are specified on the hub, the shroud, the inlet, and the exit by using Oh's technique (Ref. 9), and grid points on the hub and the shroud are connected by straight lines (in the r-z plane). The θ-values on the blade surfaces at the grid points in the r-z plane can be determined as follows. First θ is computed at the intersection points of the hub-to-shroud grid lines in the r-z plane and the streamwise-like lines along which the spline fits have been determined. Then spline fits are constructed of θ along the hub-to-shroud grid lines, and finally these spline fits are evaluated at the grid points on these lines. Given the grid in the r-z plane and θ-values on the blade surfaces at the grid points in this grid, the three-dimensional grid can be constructed by defining normalized blade-to-blade grid point distributions at the inlet and the exit (again by using Oh's technique). Grid lines in circumferential (blade-to-blade) direction correspond to constant r and z, so that the grid is automatically periodic (provided that the blade-to-blade grid point distributions have been made periodic). Splitter blades are "inserted" into the grid after their θ-coordinates have been computed (as for the main blades), while cavities are treated as extensions of the grid in the hub-to-shroud direction.

Several refinements have been included in the above procedure to allow for geometries that, strictly speaking, would not be amenable to the above approach. For example, if the blade leading edge or trailing edge is not a straight line in the r-z plane, a transformation is carried out that "straightens" this edge before the grid in the r-z plane is generated, while a back-transformation is carried out after the grid has been generated. In that case, the final hub-to-shroud grid lines projected onto the r-z plane are not straight anymore. Other refinements include rounding off of leading edges (if the data do not contain enough resolution near the leading edge) and the inclusion of a tip clearance region. Although the current procedure has its limitations, its algebraic nature ensures it is robust and fast, which allows the user to quickly optimize the grid for a given set of data.

2.4 Boundary Conditions

The computational domain chosen for the impeller/inducer calculations consisted of one passage between two (main) blades, appropriately extended upstream and downstream of these blades. On this domain, the physical boundary conditions used were as follows:

(i) No-slip and adiabatic wall conditions were specified on all solid surfaces.

(ii) Velocity profiles and total temperature were specified at the inflow boundary.

(iii) Static pressure was specified at the outflow boundary.

(iv) Periodicity conditions were applied in the circumferential direction in the impeller/inducer sections upstream and downstream of the (main) blades.

These boundary conditions were augmented by the appropriate numerical boundary conditions, viz. zero pressure gradient on stationary solid surfaces, zero reduced pressure gradient on rotating solid surfaces, extrapolation of pressure at the inflow boundary, and extrapolation of velocities and temperature at the outflow boundary.

2.5 Initial Conditions

In the impeller/inducer calculations, a steady-state solution was sought in the rotating frame of reference. Therefore, the initial conditions applied to these calculations serve as an initial guess, and do not affect the converged steady-state solution (although they will, in general, affect the convergence history). In the present calculations, an initial guess was obtained as follows:

(a) The velocity vector was aligned everywhere with the "streamwise" grid lines.

(b) The velocity magnitude in a given cross-section was determined from the (estimated) cross-sectional area and one-dimensional mass conservation.

(c) The static pressure distribution was obtained from the assumption of constant rothalpy along a "streamwise" grid line.

No attempt was made to include boundary layer profiles in the initial guess.

2.6 Impeller/Inducer Calculations

Several aspects of the algorithm are of importance when running impeller/inducer calculations, viz. the matrix preconditioning, the artificial dissipation, and the treatment of incompressible flows. Each of these aspects will be discussed below.

Matrix Preconditioning

The numerical algorithm described in Section 2.2 can be used to obtain both time-dependent and steady-state solutions. If a steady-state solution is sought, matrix preconditioning can be applied to speed up convergence and improve stability limits. This preconditioning is based on an

approximate eigenvalue analysis, and, as such, assumes that the specified reference length and velocity scale are indeed representative physical quantities. If this is not the case, the preconditioning may not be successful, and the convergence rate may be (unacceptably) slow. An example of this behavior was encountered during the first inducer calculation, in which a reference length scale of 1 inch and a reference velocity scale of 1 ft/s were used. Even after 6000 iterations, the solution had not yet converged! By choosing a proper length scale (the tip diameter) and a proper velocity scale (the tip speed) the problem was resolved, and a converged solution was obtained in about 1000 iterations.

Artificial Dissipation

Use of artificial dissipation (cf. Section 2.2) tends to enhance the stability and convergence properties of the numerical solution procedure, but it also tends to reduce the accuracy of the solution, in particular on coarse grids. Therefore, the impeller and inducer calculations were performed with an initial value of the artificial dissipation coefficient $\sigma_d = 0.5$ (corresponding to full artificial dissipation). After the flow field had been established, this coefficient was reduced to $\sigma_d = 0.2$. This reduction of artificial dissipation did not affect the flow field qualitatively (and did not significantly affect the flow split in impellers with splitter blades), but it did increase the pressure rise through the inducer or impeller, and also the efficiency.

Treatment of Incompressible Flow

The constant-density flow field obtained from the incompressible Navier-Stokes equations is equivalent to the flow field obtained from the compressible Navier-Stokes equations if the Mach number tends to zero. The error introduced by using a nonzero Mach number M is $O(M^2)$, so that an accurate approximation to the incompressible flow field can be obtained from a compressible flow field calculation provided that the Mach number is sufficiently small. This can be accomplished by adjusting some of the compressible flow parameters. For example:

(i) Choose a (small) molecular weight that, for the given reference temperature, yields a sufficiently high speed of sound.

(ii) Let the reference pressure be equal to the downstream static pressure. Then the gas law yields a reference density, say ρ_{ref}. This reference density will in general be much smaller than the actual liquid density ρ_{liq}.

(iii) Multiply the liquid viscosity μ_{liq} by ρ_{ref}/ρ_{liq} to ensure that the Reynolds number used in the compressible flow equations is not changed by using the density ρ_{ref} rather than ρ_{liq}.

Because for low Mach numbers the energy equation is effectively decoupled from the continuity and momentum equations, these latter equations yield a velocity field and a pressure coefficient that are independent of the value of ρ_{ref} used (provided that the Reynolds number is kept the same when ρ_{ref} is changed).

The approach followed in the inducer/impeller calculations was to start with a Mach number of about 0.3, and switch to a lower Mach number (0.1 or 0.03) after the flow field had been established (to avoid some of the convergence penalties associated with the lower Mach numbers). In none of the cases run, lowering the Mach number had a significant effect on the solution.

3. RESULTS

The work presented here was generated as part of SRA's effort under the NASA/MSFC Pump Stage Technology Team. Much of the work, including detailed comparisons with data and with the results of other investigators on the team, has been presented at NASA MSFC meetings. Details of the comparisons among the various investigators have been presented by Garcia et al. (Refs. 2-5). These details have not been repeated here. Instead, a description is given of the different cases run, with a selection of representative results.

3.1 Inducer Simulations

The first component considered was the Rocketdyne inducer (see Fig. 1). SRA's effort here was part of an effort to compare the results of several computational groups, including SECA, Aerojet, Rocketdyne, SRA, NASA Lewis Research Center, and NASA Ames Research Center, both with each other and with Rocketdyne data. The relevant inducer parameters are given in Table 1. The radial and tangential inflow velocities were taken to be zero, while the axial inflow velocity was taken to be constant. Boundary layer profiles were added to satisfy the no-slip condition at the inlet.

Tip diameter	6.0 inch
Inlet hub diameter	1.8 inch
Discharge hub diameter	3.6 inch
Number of blades	6
Design speed	3600 rpm
Design flow rate	2236 gpm
Inlet design flow coefficient	0.3

Table 1. Rocketdyne Inducer Parameters

The SRA simulation was run with a grid containing about 300,000 grid points (121 grid points in the streamwise direction, 41 grid points from hub to end wall and 61 grid points from blade to blade). Figure 2 shows the grid at the mid-span blade-to-blade surface. For clarity, only every other axial station has been shown. The clustering of grid points near the blade surfaces and the helical-like extensions of the grid upstream and downstream of the blades (as described in Section 2.3) are clearly visible. Although the calculations were performed with a stationary shroud (in the absolute frame of reference), so that there was relative motion between the shroud and the blades, the tip clearance was assumed to be zero, and no leakage was considered. As discussed in Section 2.6, convergence problems were encountered at first, which, as it turned out, were due to the use of improper length and velocity scales. A fully converged solution was obtained only after the length scale was set equal to the tip diameter and the velocity scale was set equal to the tip speed. Figures 3 and 4 show some representative results. In these figures (and all subsequent figures), the velocity has been nondimensionalized by the tip speed, and the pressure coefficient is based on the dynamic pressure that corresponds to the tip speed. Figure 3, which shows the pressure coefficient in the mid-span blade-to-blade surface, clearly illustrates the blade loading and the pressure rise across the inducer. Figure 4 shows the velocity magnitude in transverse grid surfaces just behind the leading edge, in the middle of the inducer, and just ahead of the trailing edge. In this last surface, flow distortion is clearly visible.

3.2 Impeller Simulations

A number of impeller configurations was considered under the present program. These included: (a) the Baseline STME Impeller, (b) the Optimized STME Impeller with different splitter

lengths, and (c) the SSME HPFTP Impeller. Each of these impeller configurations is discussed below.

STME Impellers

In the course of the program, four STME impeller geometries were furnished by Rocketdyne: a baseline design and an optimized design with three different splitter blade lengths. The "optimized" impeller was designed by Rocketdyne after the baseline impeller results had been obtained by the various groups (including SRA). After the flow field had been computed for this optimized impeller, it was decided to perform parametric studies on several aspects of the impeller geometry, in order to further improve its performance. Different geometric variations were assigned to the different groups (see Ref. 5); SRA's task was to study the effect of splitter blade length. For this purpose, Rocketdyne provided two additional splitter blade geometries, denoted as the "long" splitter and the "longer" splitter. The "long" splitter was extended over 1/3 of the distance between the leading edge of the original splitter and the impeller leading edge; the "longer" splitter was extended over 2/3 of this distance. Table 2 lists some relevant impeller parameters that are the same for all configurations studied. It should be noted that the B2-width of the optimized impeller was larger than that of the baseline design (0.712 inch vs. 0.64 inch for the water test models). Circumferentially averaged inflow conditions were also specified by Rocketdyne; they were the same for all three optimized impeller configurations, but these conditions differed from those specified for the baseline impeller, as can be seen in Figs. 5 and 6.

Inlet tip diameter	6.0 inch
Inlet hub diameter	3.9 inch
Impeller tip diameter	9.045 inch
Number of blades	6 + 6
Design speed	6322 rpm
Design flow rate	1210 gpm
Inlet design flow coefficient	0.144

Table 2. STME Impeller Parameters (Water Test Conditions).

The impeller geometries are shown in Figs. 7-10. Although it is difficult to see the differences between the baseline impeller geometry and the optimized impeller geometry (Figs. 7-10), the differences in the splitter lengths of the three optimized impeller geometries is clearly visible (Figs. 8-10). Each geometry was run on a grid containing about 160,000 grid points (121 in the streamwise direction, 51 in the blade-to-blade direction, and 26 in the hub-to-shroud direction). Figure 11 shows the grid for the optimized impeller in the mid-span blade-to-blade surface. Only every other streamwise station is shown. The clustering of the grid lines near the blade (both the full blades and the splitters) is clearly visible. All calculations were basically run the same way. The end wall upstream of the impeller leading edge was taken to be stationary, and a "gap" region was included between this end wall and the impeller shroud (which was attached to the blades). Downstream of the impeller trailing edge, the hub and end wall were treated as slip boundaries to better simulate the actual geometry (which included a sudden expansion downstream of the trailing edge). Results of the computations are shown in Figs. 12-23. Additional results can be found in Refs. 5 and 10. The plots of the pressure coefficient in the mid-span blade-to-blade surface (Figs. 12-15) show the pressure rise through the impellers and the loading on the different blades. Careful examination of these figures shows that the pressure rise through the optimized impeller is larger than that through the baseline impeller. For both impellers, the splitter blades are loaded less than the full blades, but for the baseline impeller the difference is larger. Increasing the splitter length increases the loading on the splitter blades, and decreases the loading on the full blades. For the impeller with the "longer" splitter, the loading of a splitter blade is significantly higher than that of a full blade! The plots of the velocity magnitude in the mid-span blade-to-blade surface (Figs. 16-18) show the development of (large) regions of low velocity near the suction sides of all blades. For the baseline and the optimized impeller, the low velocity regions are larger near the full blades than near the splitter blades (with again the difference being more significant for the baseline impeller than the optimized impeller). For the optimized impellers with the "long" and "longer" splitter blades, the situation is reversed! These results are in agreement with the computed mass fluxes through the different passages, as shown in Table 3 below.

Clearly, the optimized impeller has a more even mass flow split than the other impellers. This has also been illustrated in Figs. 20-23, which show the velocity magnitude in streamwise sections just ahead of the splitter leading edge, midway between the splitter leading edge and the impeller trailing edge, and just ahead of the impeller trailing edge. The development of the low velocity regions and their size near the impeller trailing edge are clearly visible, and agree with the results mentioned above. All of these results indicate that the optimized impeller is the best one, and that although lengthening the splitter blade may improve the impeller performance, only a small amount of lengthening will be required.

	Percentage of Mass Flux in Passage Between Full Blade Pressure Side and Splitter Suction Side	Percentage of Mass Flux in Passage Between Splitter Pressure Side and Full Blade Suction Side
Baseline	56%	44%
Optimized	52%	48%
Optimized with "Long" Splitter	46%	54%
Optimized with "Longer" Splitter	44%	56%

Table 3. STME Impeller Mass Flow Splits.

Finally, it should be pointed out that several calculations were performed on the optimized impeller to assess the effect of specific computational treatments. For example, the "gap" region on the end wall upstream of the impeller leading edge was reduced to zero, the downstream hub and end wall were treated as solid walls (rather than slip boundaries), and the boundary layer thickness at the inflow plane was increased. None of these treatments affected the results significantly, although the treatment of the hub and end wall downstream of the trailing edge did significantly affect the flow behavior in that region (see also the discussion in the next section). A change of the inflow conditions provided by Rocketdyne, however, proved to have major impact.

SSME HPFTP Impeller

The final case considered was the SSME impeller. After the calculations were performed, data became available for this simulation and hence, the case served as a code validation simulation. The configuration (shown in Fig. 24) was again specified by Rocketdyne. This configuration has an attached shroud, two sets of splitter blades, and a sudden expansion downstream of the impeller trailing edge.

Inlet tip diameter	6.35 inch
Inlet hub diameter	3.95 inch
Impeller tip diameter	11.0 inch
Impeller B2 width	0.589 inch
Number of blades	6 + 6 + 12
Design speed	6322 rpm
Inlet design flow coefficient	0.256

Table 4. SSME Impeller Parameters (Water Test Conditions).

Grids were generated and simulations were run both with and without this sudden expansion. The initial calculations were performed on the geometry without the sudden expansion of the flow passage downstream of the impeller trailing edge on a grid consisting of about 192,000 points: 121 points in the streamwise direction, 61 points from blade to blade (corresponding to 15 mesh cells in each of the four passages formed by the main blades, the long partial blades, and the short partial blades), and 26 points from hub to shroud. At the inflow boundary, the axial and circumferential velocity components were obtained by interpolating the Rocketdyne test data; the radial velocity component was set to zero (because no data was available). Upstream of the impeller leading edge, the hub was rotating, while the end wall was stationary (with a small "gap" between the end wall and the impeller leading edge). Downstream of the impeller trailing edge, the "hub" and "shroud" surfaces were treated as "slip" surfaces. The calculations on the actual test configuration (including the sudden expansion) were performed on a slightly refined grid with 81 points from blade to blade (instead of 61 points) and with an additional 10 points in the hub-to-shroud direction in each cavity. Since each cavity contained 16 grid points in the streamwise direction, the total number of "active" grid points was about 278,000.

Figure 25 shows the corresponding grid at the mid-span blade-to-blade surface (with, again, every other streamwise station removed). Two calculations were performed on this geometry: in the first of these, the cavity walls were rotating, while in the second one, the cavity walls were stationary (with a small "gap" between these walls and the rotating hub and shroud at the impeller trailing edge). In both cases, the hub and end-wall surfaces downstream of the cavities were treated as "slip" boundaries. The last calculation (with the non-rotating expansion) is the one that most closely resembles the actual geometry.

The results of the three calculations are shown in Figs. 26-36. Again, the plots of the pressure coefficient in the mid-span blade-to-blade surface (Figs. 26-28) show the blade loading

and the pressure rise through the impeller. The full blades are loaded the most, while the short splitters are loaded the least, as one would expect. The plots of the velocity magnitude (Figs. 29-31) clearly show the differences between the four passages: near the impeller exit there is a large low-velocity region in the passage near the full blade suction side, the velocity distributions in the passages on either side of the long splitter are very similar, and the velocities are high in the passage near the pressure side of the full blade. The same conclusions can be drawn from Figs. 32-34, which show the velocity magnitude at streamwise locations just ahead of the long splitter leading edge, just ahead of the short splitter leading edge, and just ahead of the impeller trailing edge. The mass flow splits (which are essentially the same for all three cases) also confirm the above results (see Table 5).

Passage Between Full Blade Pressure Side and Short Splitter Suction Side	Passage Between Short Splitter Pressure Side and Long Splitter Suction Side	Passage Between Long Splitter Pressure Side and Short Splitter Suction Side	Passage Between Short Splitter Pressure Side and Full Blade Suction Side
30%	26%	24%	20%

Table 5. SSME Impeller Flow Splits.

Figures 26-34 show that there are no major differences in the flow through the impeller between the three cases considered, although a careful examination of Figs. 29-34 does show some minor differences near the impeller exit (as one would expect). The flow downstream of the trailing edge, however, shows significant differences, because the recirculation regions in the cavities affect the overall flow picture. As can be seen from Figs. 35 and 36, this effect is larger when the cavities are stationary. In that case, the recirculation zones are stronger, the flow distortion near the impeller trailing edge due to this recirculation zone is more pronounced, and a region of reverse flow develops near the end wall downstream of the expansion. These results indicate that in order to compare calculated results with experimental data downstream of the trailing edge, the geometry downstream of the trailing edge must be modeled properly.

4. CONCLUSIONS

Under the present effort, a three-dimensional Navier-Stokes code was used for various inducer and impeller flow field calculations. An existing algebraic grid generation procedure was extended to allow for nonzero blade thickness, splitter blades, and hub/shroud cavities upstream or downstream of the (main) blades, resulting in a fast, robust inducer/impeller geometry/grid generation package. Problems associated with running a compressible flow code to simulate an incompressible flow were resolved; related aspects of the numerical algorithm (viz., the matrix preconditioning, the artificial dissipation, and the treatment of low Mach number flows) were addressed. As shown by the calculations performed under the present effort, the resulting code, in conjunction with the grid generation package, is an effective tool for the rapid solution of three-dimensional viscous inducer and impeller flows.

REFERENCES

1. McConnaughey, P.K. and Schutzenhofer, L.A.: "Overview of the NASA/MSFC CFD Consortium for Applications in Propulsion Technology," AIAA Paper 92-3219, AIAA/SAE/ ASME/ASEE 28th Joint Propulsion Conference and Exhibit, July 1992.

2. Garcia, R., Jackson, E.D., and Schutzenhofer, L.A.: "A Summary of the Activities of the NASA/MSFC Pump Stage Technology Team," Proceedings of the Fourth International Symposium on Transport Phenomena and Dynamics of Rotating Machinery, April 1992.

3. Garcia, R., McConnaughey, P.K., and Eastland, A.H.: "Activities of the NASA/Marshall Space Flight Center (MSFC) Pump Stage Technology Team," AIAA Paper 92-3222, AIAA/SAE/ASME/ASEE 28th Joint Propulsion Conference and Exhibit, July 1992.

OK ✓4. Garcia, R., Williams, R. and Dakhoul, Y.: "A Status of the Activities of the NASA/MSFC Pump Stage Technology Team," Tenth Workshop for Computational Fluid Dynamic Applications in Rocket Propulsion, NASA CP 3163, Part I, 1992, pp. 173-200.

5. Garcia, R., McConnaughey, P. and Eastland, A.: "Computational Fluid Dynamics Analysis for the Reduction of Impeller Discharge Flow Distortion," AIAA Paper 94-0749, 32nd Aerospace Sciences Meeting & Exhibit, January 1994.

6. Briley, W.R. and McDonald, H.: 'Solution of the Multidimensional Compressible Navier-Stokes Equations by a Generalized Implicit Method," *J. Computational Physics*, Vol. 24, 1977, pp. 372-397.

7. Briley, W.R. and McDonald, H.: "On the Structure and Use of Linearized Block Implicit Schemes," *J. Computational Physics*, Vol. 34, 1980, pp. 54-72.

8. Govindan, T.R., de Jong, F.J., Briley, W.R. and McDonald, H.: "Rotating Flow in Radial Turbomachinery," SRA Final Report, U.S. Army Research Office Contract DAAG29-85-C-0030, May 1990.

9. Oh, Y.H.: "An Analytical Transformation Technique for Generating Uniformly Spaced Computational Mesh," Numerical Grid Generation Techniques, NASA CP 2166, 1980, pp. 385-398.

10. de Jong, F.J., Choi, S-K., Govindan, T.R., and Sabnis, J.S.: "Computation of the Flow Field in a Centrifugal Impeller with Splitter Blades," Tenth Workshop for Computational Fluid Dynamic Applications in Rocket Propulsion, NASA CP 3163, Part 1, 1992, pp. 245-258.

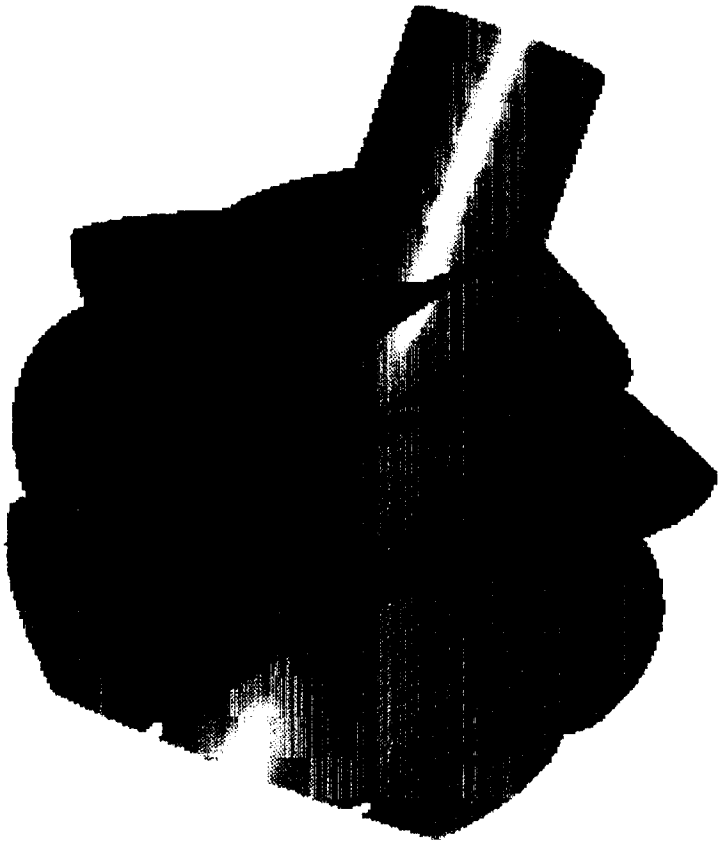

Inducer

Figure 1. Rocketdyne Inducer.

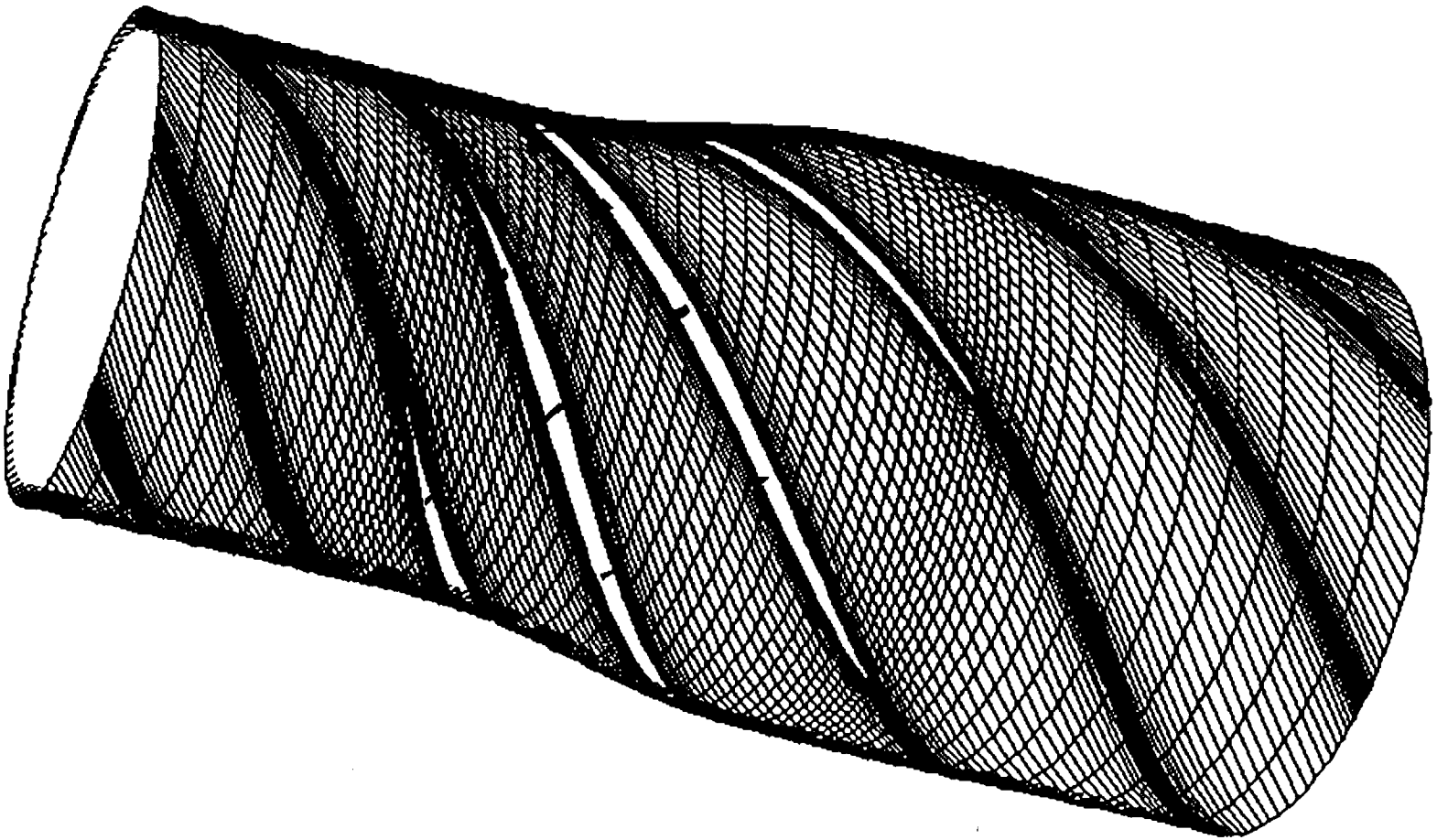

Figure 2. Inducer Grid at Mid-Span.

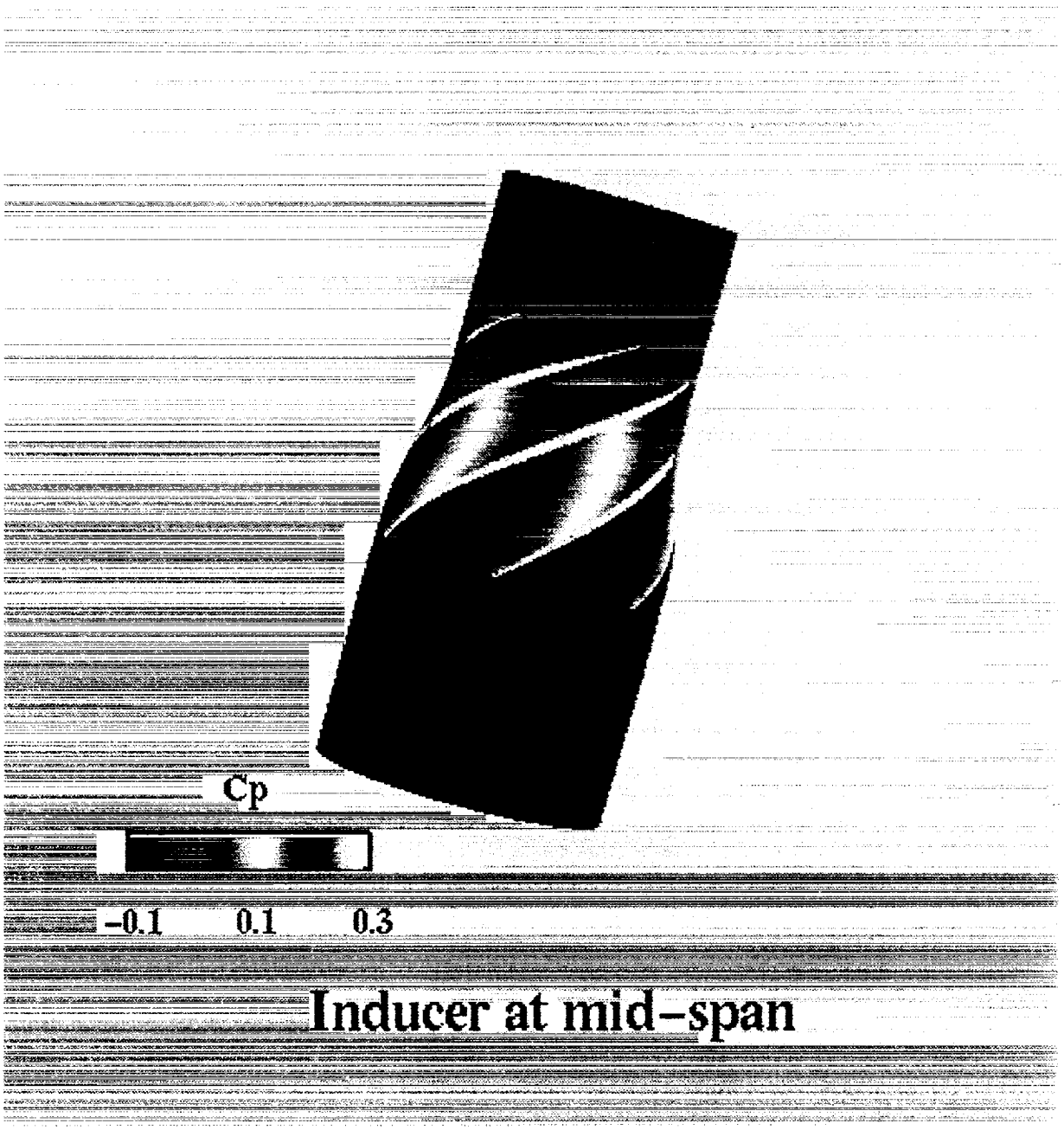

Figure 3. Inducer: Pressure Coefficient at Mid-Span.

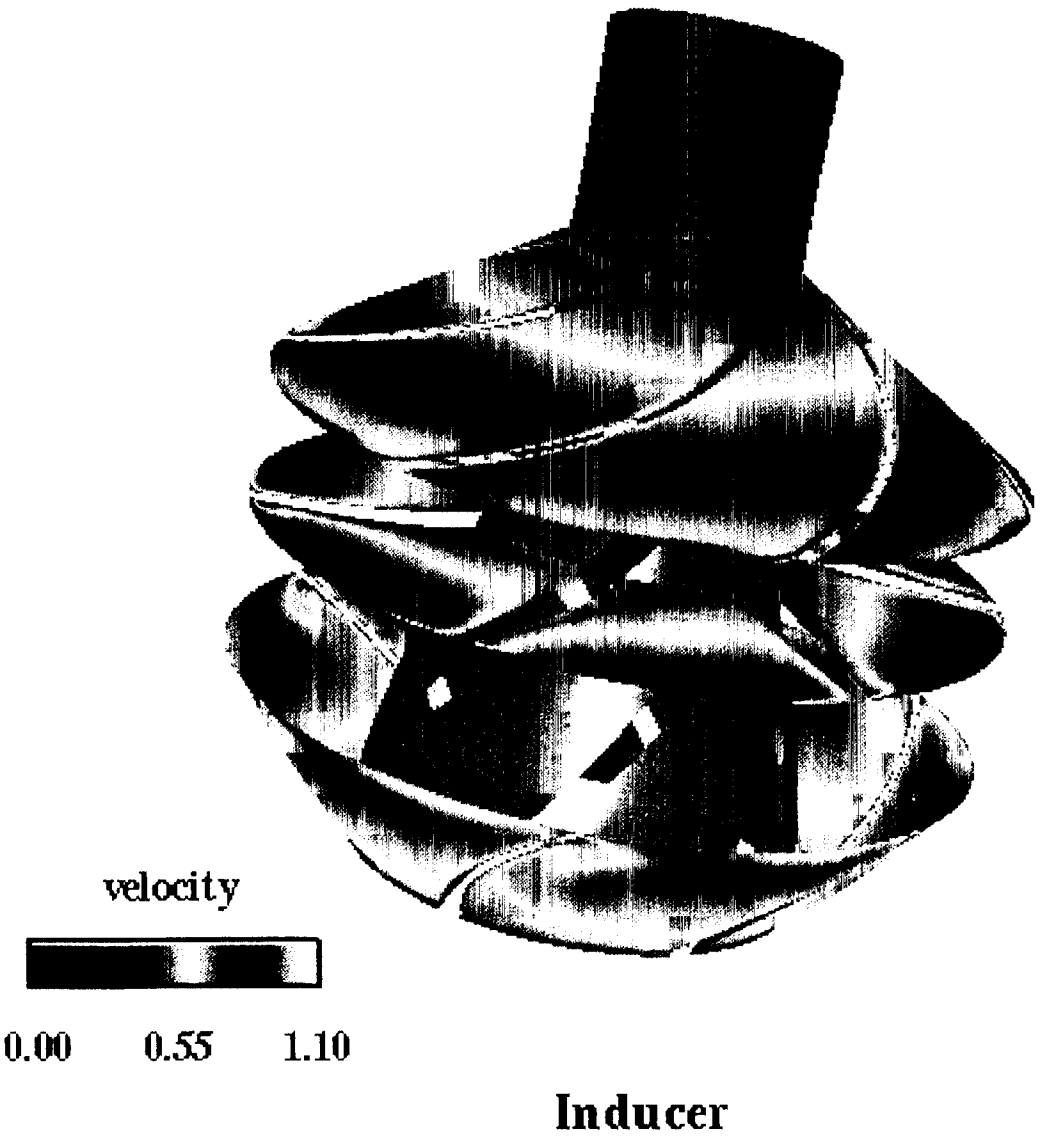

Figure 4. Inducer: Velocity Magnitude at Three Transverse Grid Surfaces.

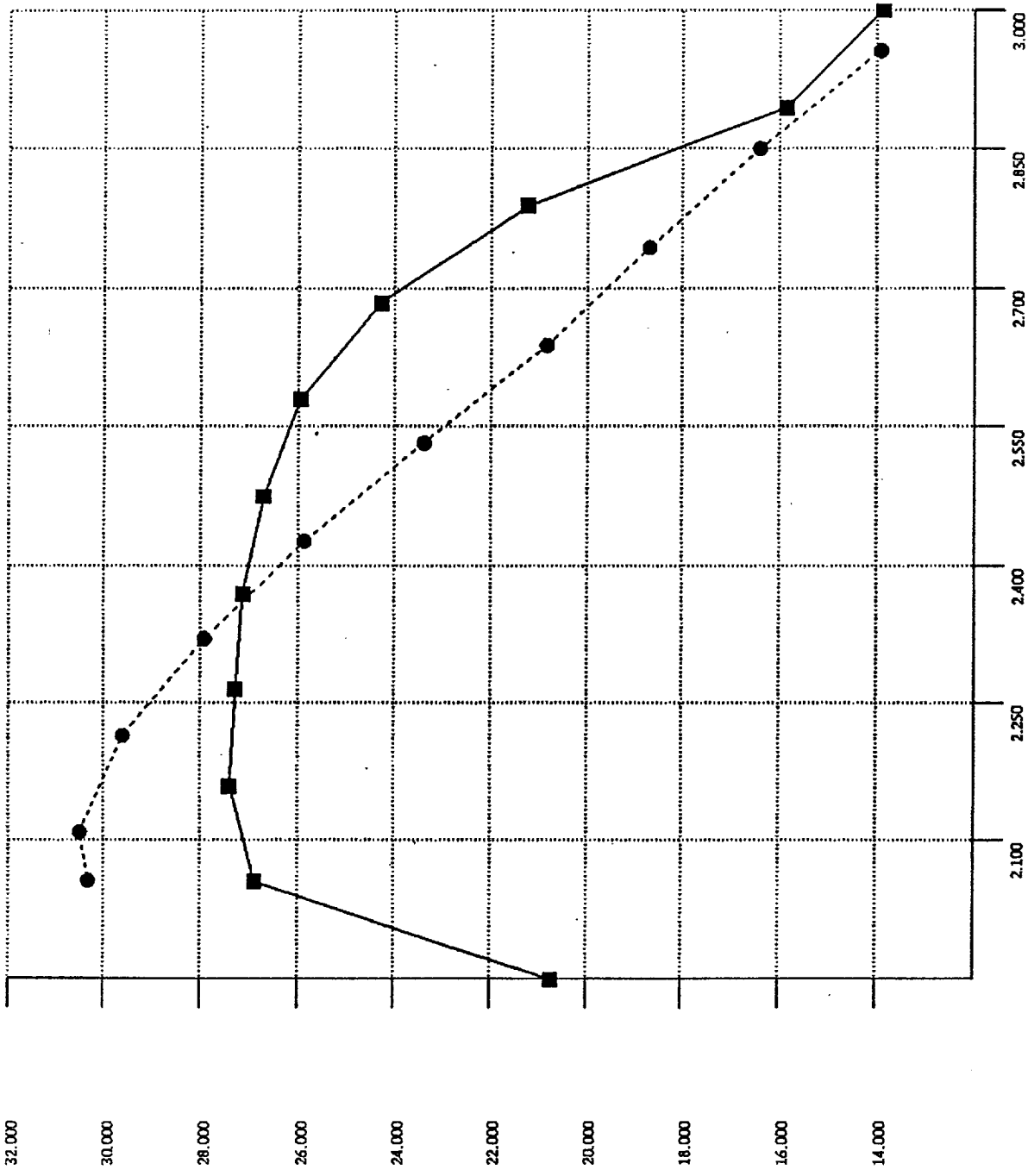

Figure 5. STME Impeller: Circumferentially Averaged Inlet Axial Velocity (ft/s) as a Function of Radius (inch).

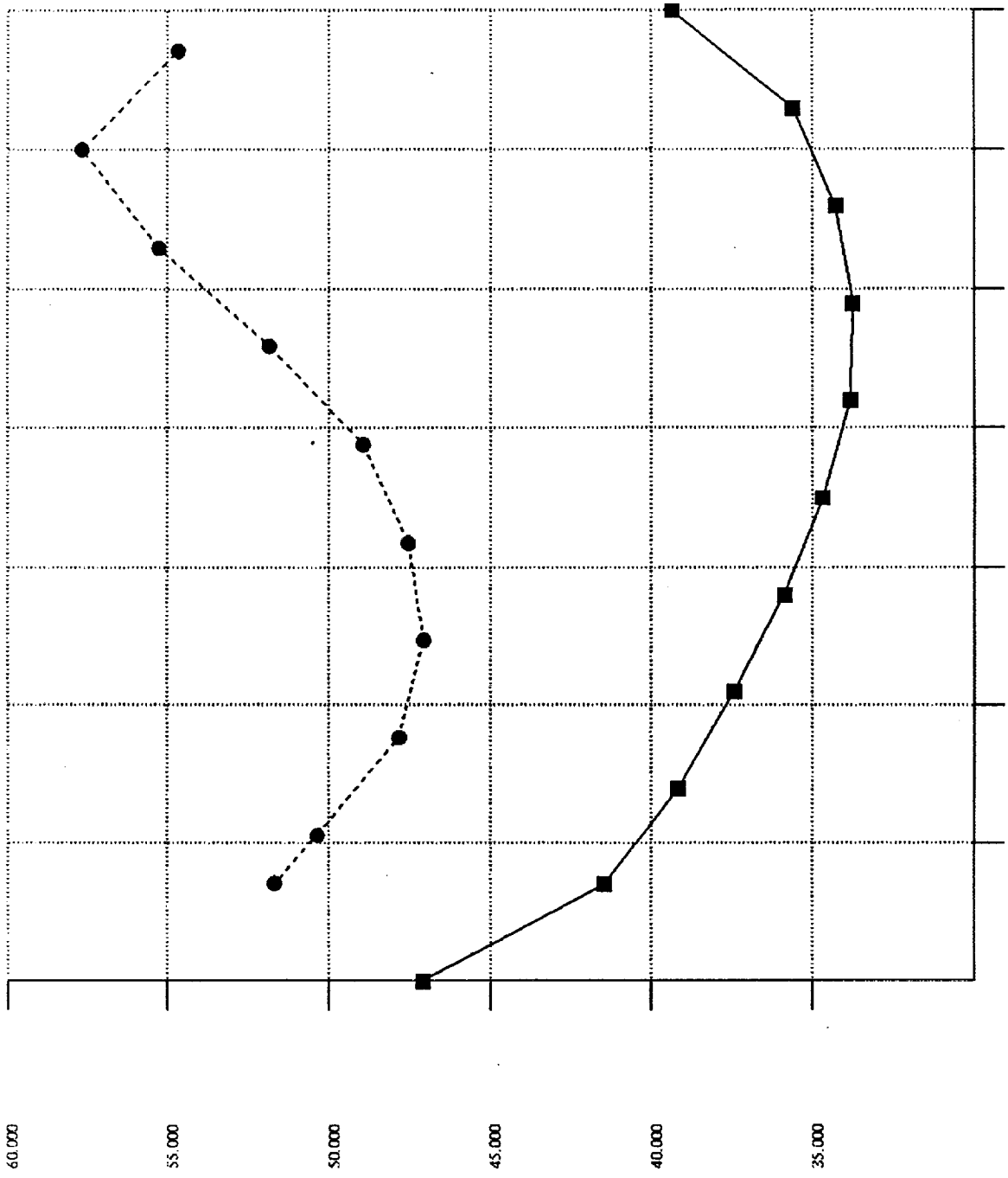

Figure 6. STME Impeller: Circumferentially Averaged Inlet Tangential Velocity (ft/s) as a Function of Radius (Inch).

Figure 7. Baseline STME Impeller.

Figure 8. Optimized STME Impeller.

Figure 9. Optimized STME Impeller with "Long" Splitter.

Figure 10. Optimized STME Impeller with "Longer" Splitter.

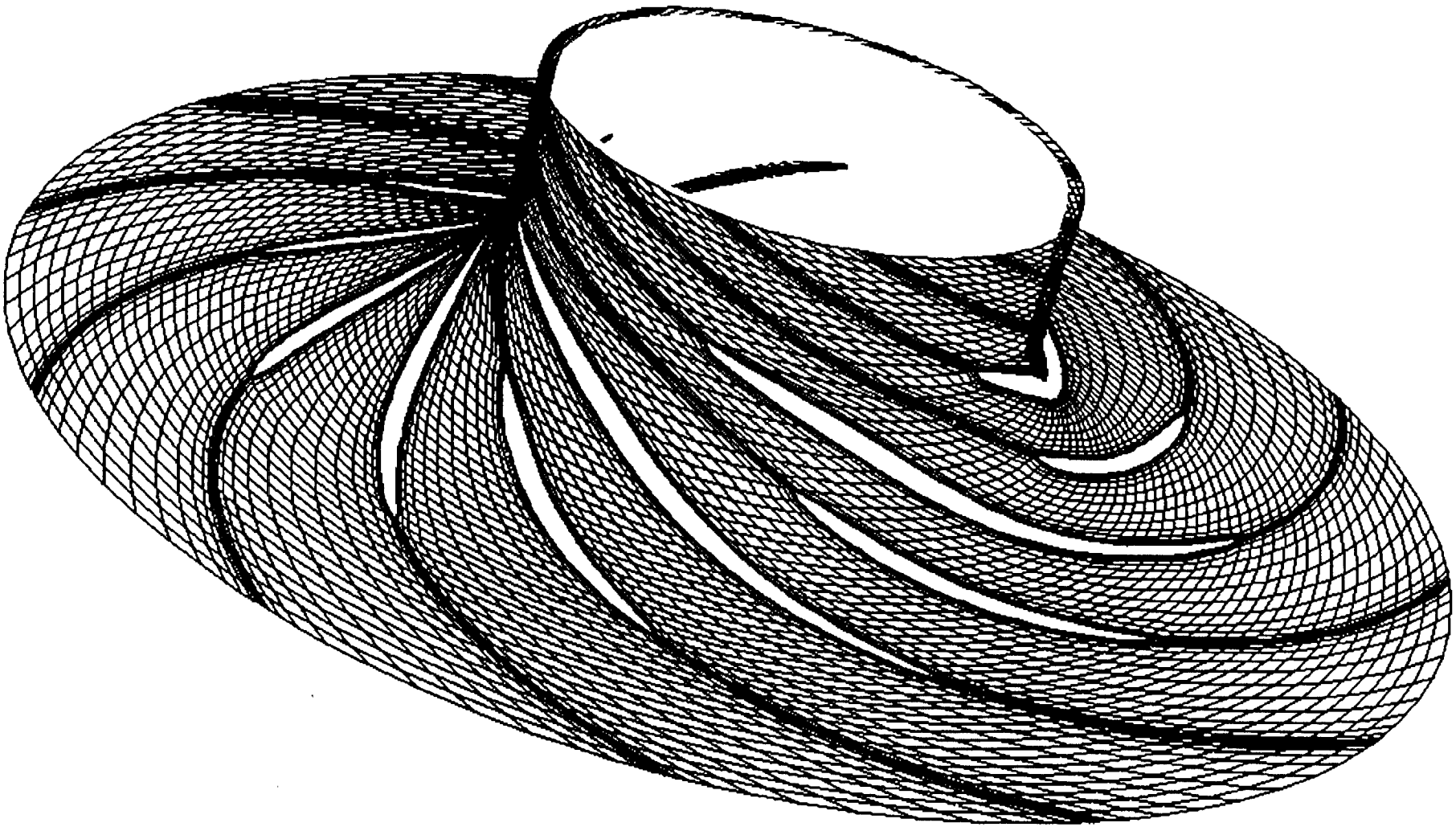

Figure 11. Optimized Impeller Grid at Mid-Span.

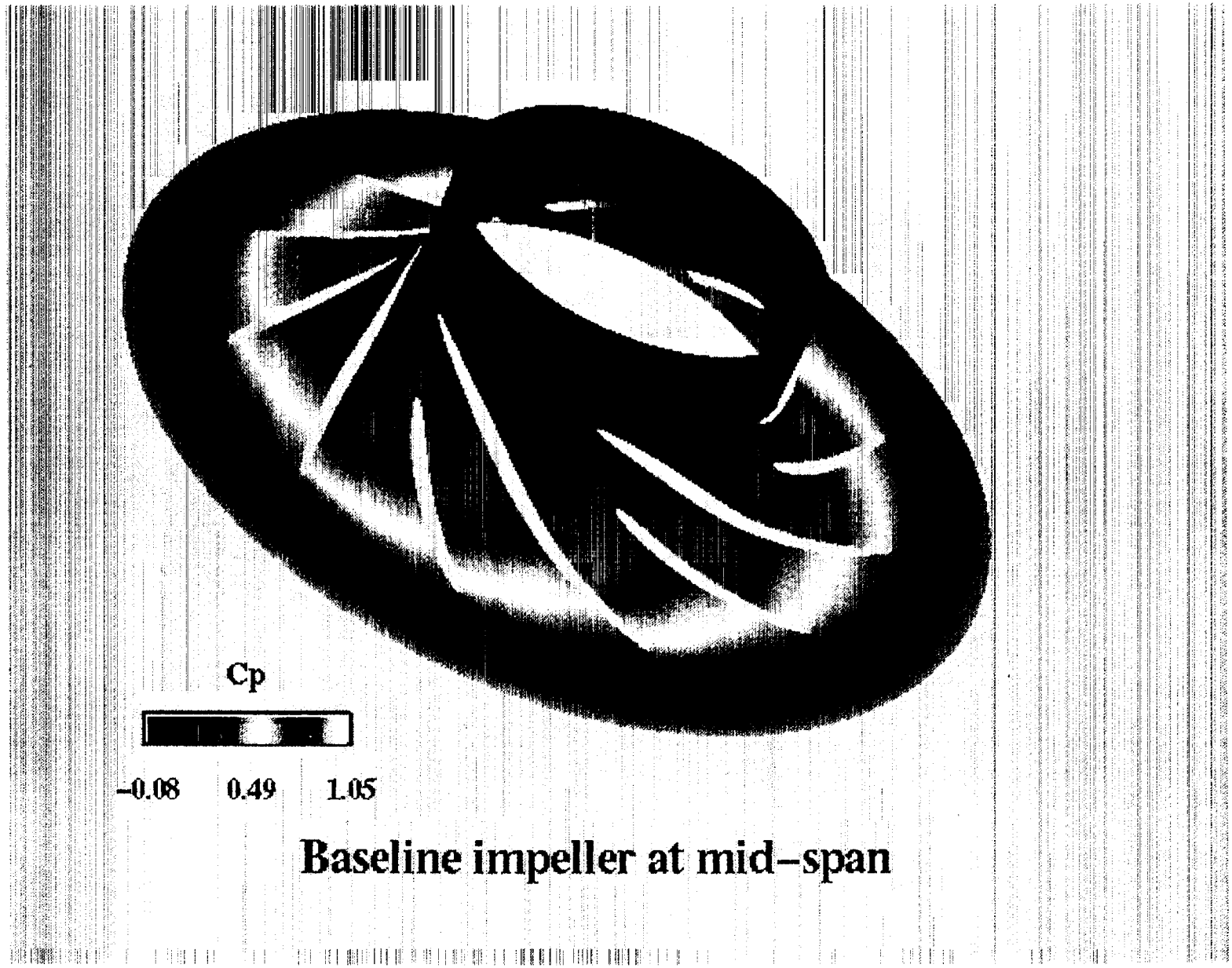

Figure 12. Baseline Impeller: Pressure Coefficient at Mid-Span.

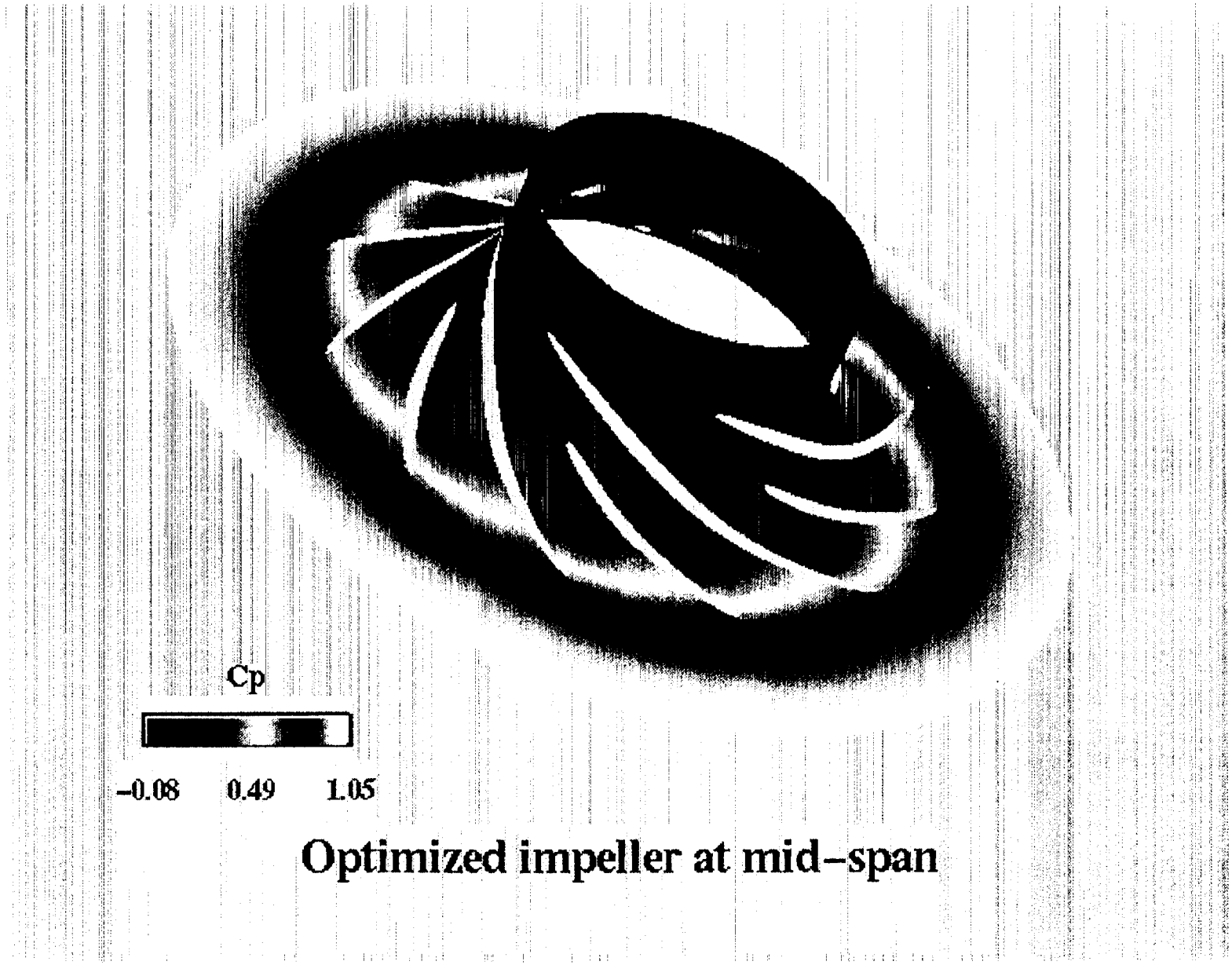

Figure 13. Optimized Impeller: Pressure Coefficient at Mid-Span.

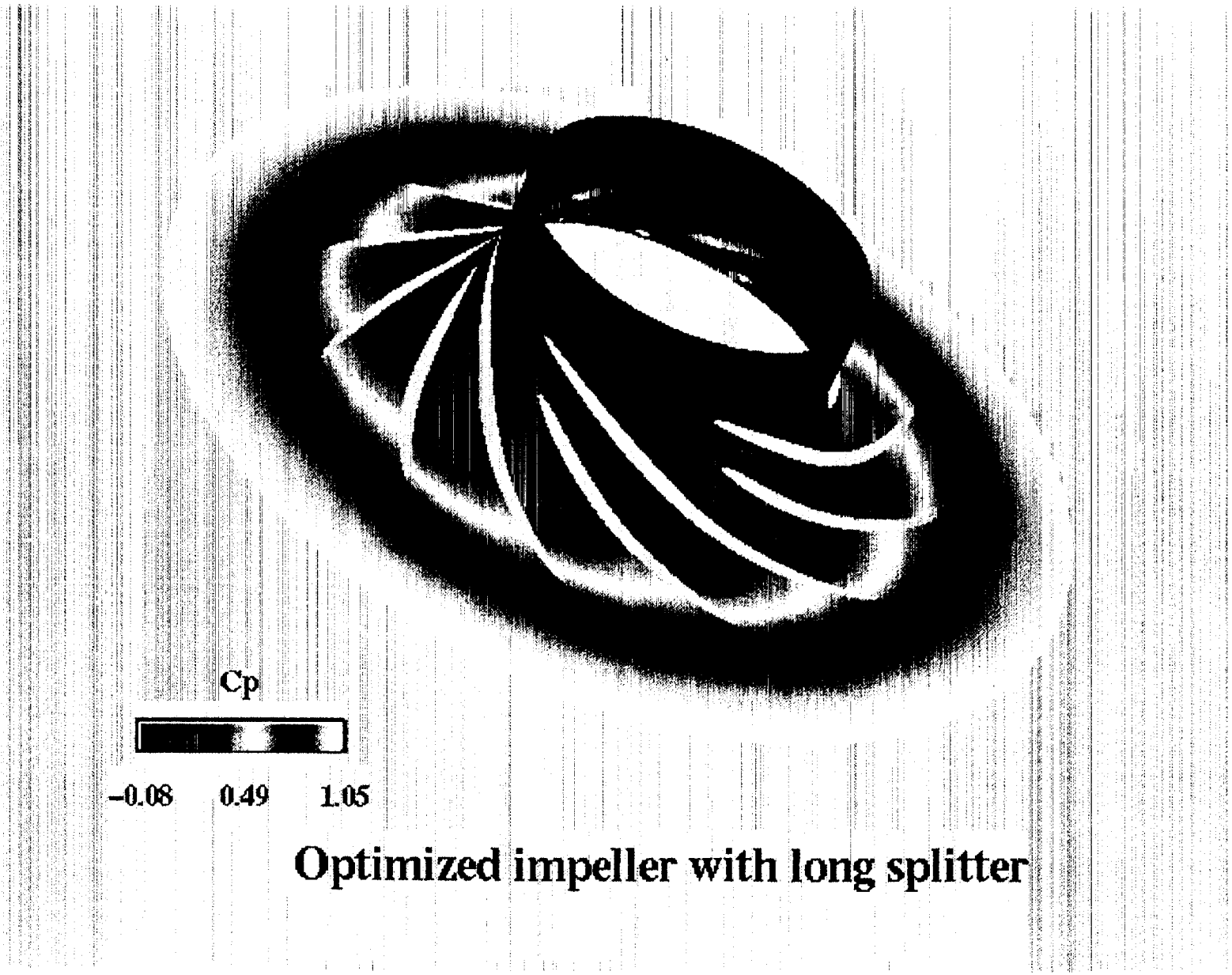

Figure 14. Optimized Impeller with "Long" Splitter: Pressure Coefficient at Mid-Span.

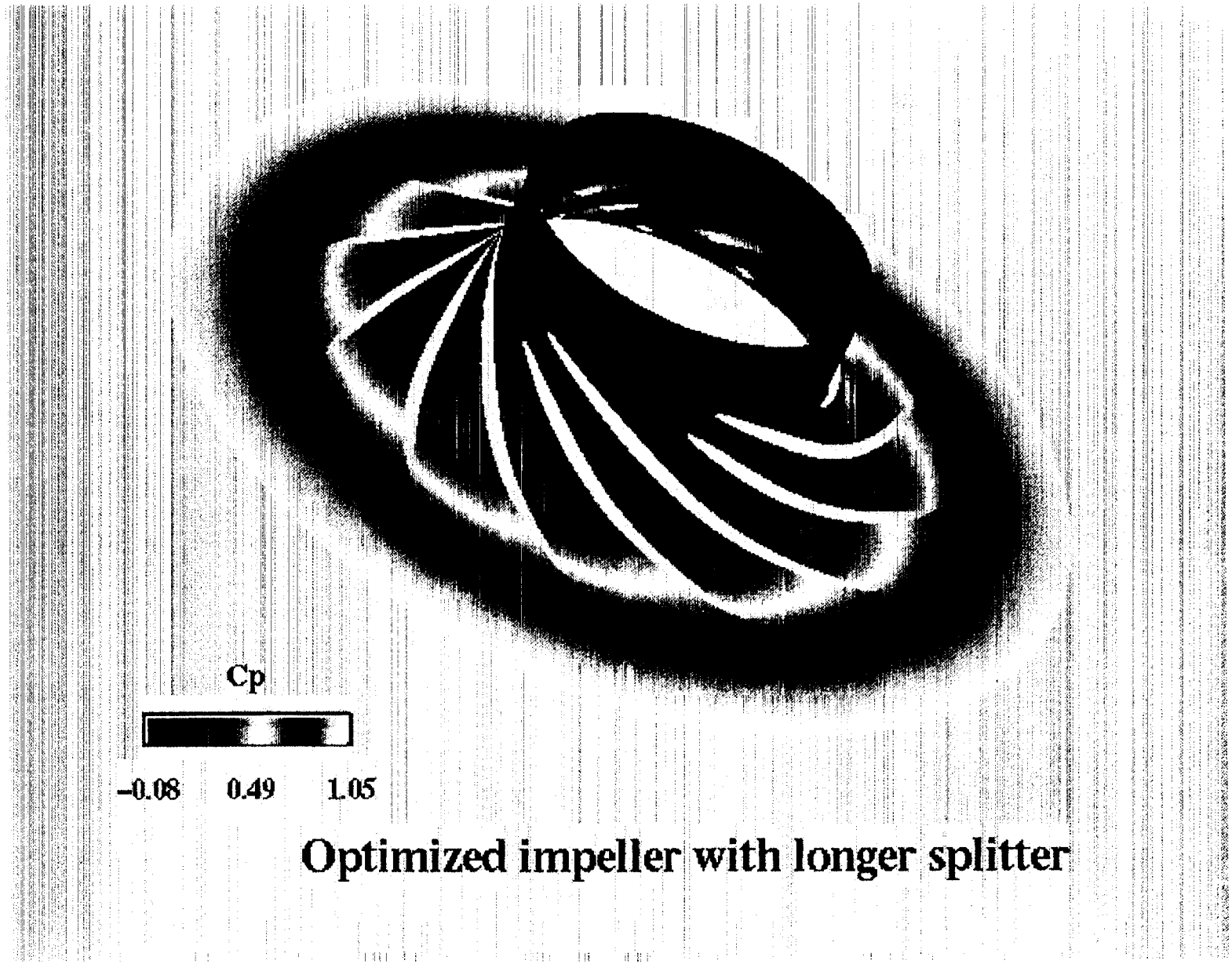

Figure 15. Optimized Impeller with "Longer" Splitter: Pressure Coefficient at Mid-Span.

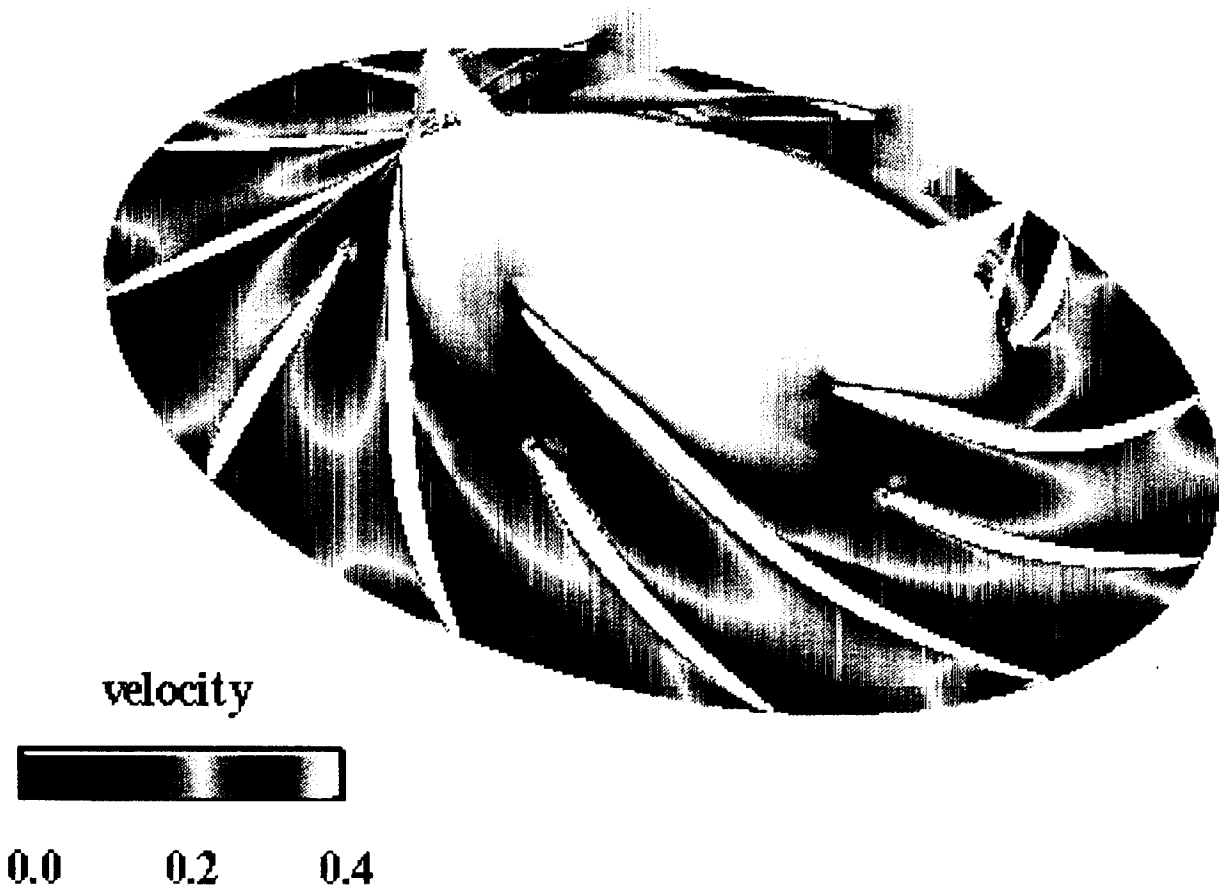

Figure 16. Baseline Impeller: Velocity Magnitude at Mid-Span.

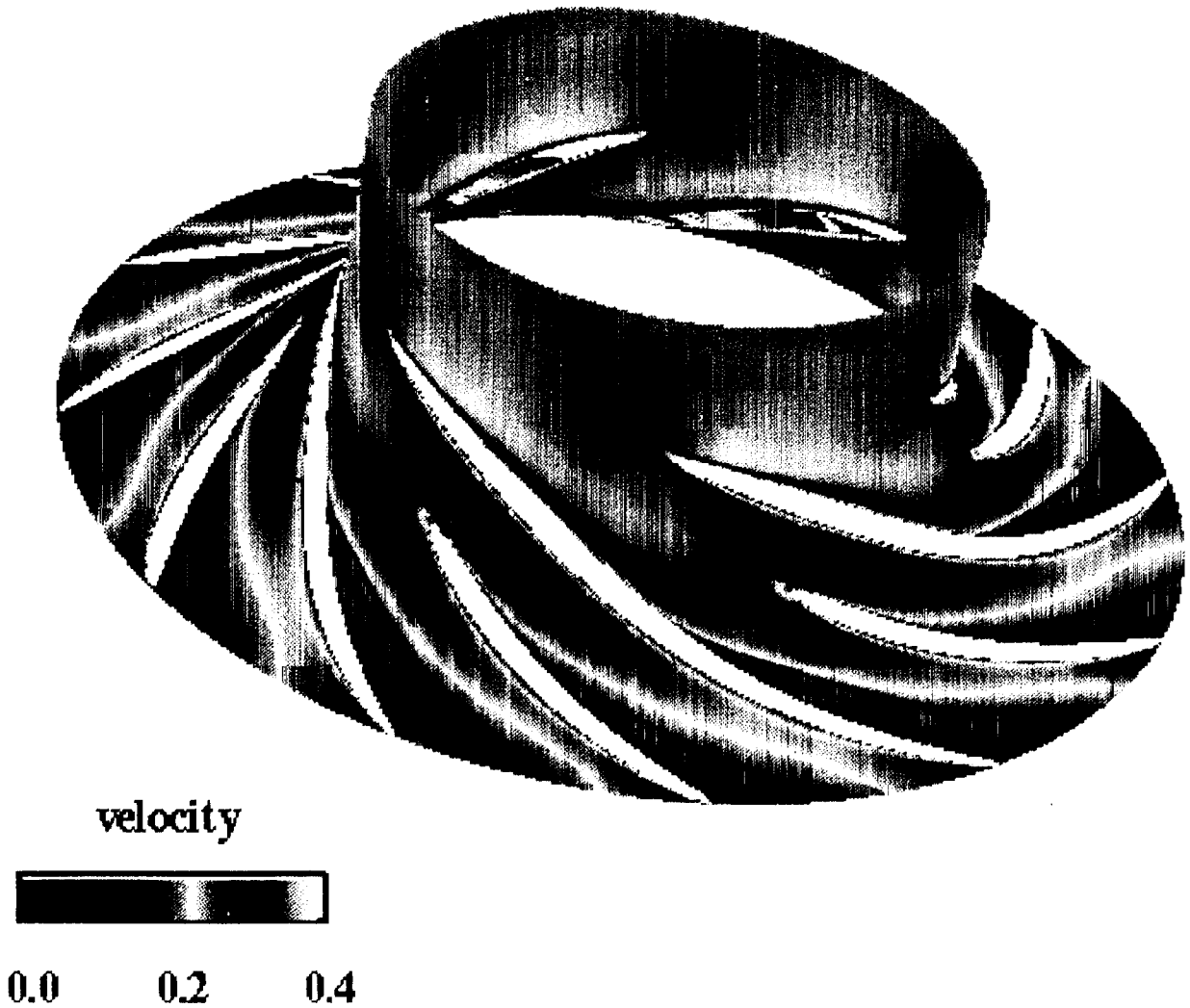

Figure 17. Optimized Impeller: Velocity Magnitude at Mid-Span.

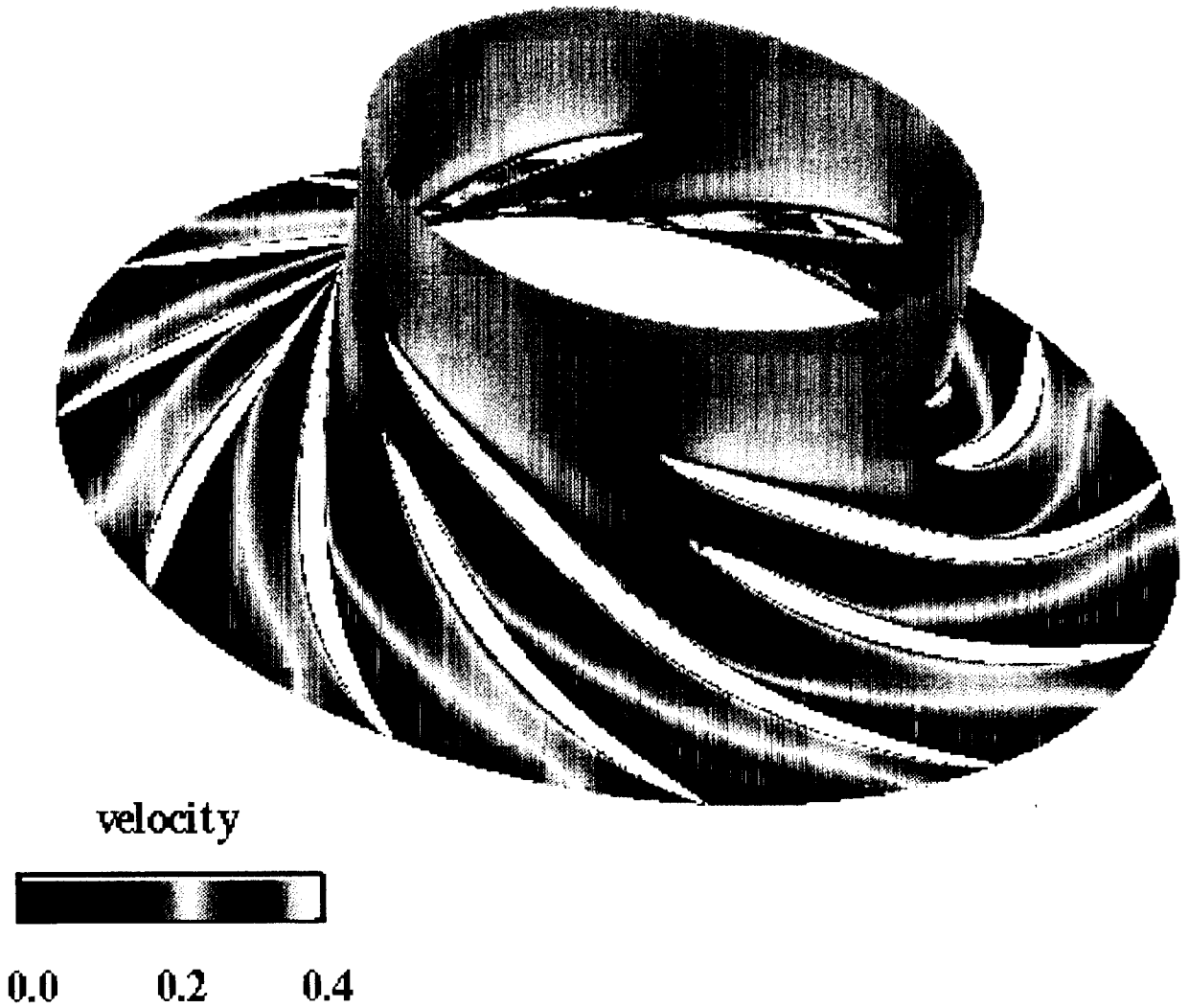

Figure 18. Optimized Impeller with "Long" Splitter: Velocity Magnitude at Mid-Span.

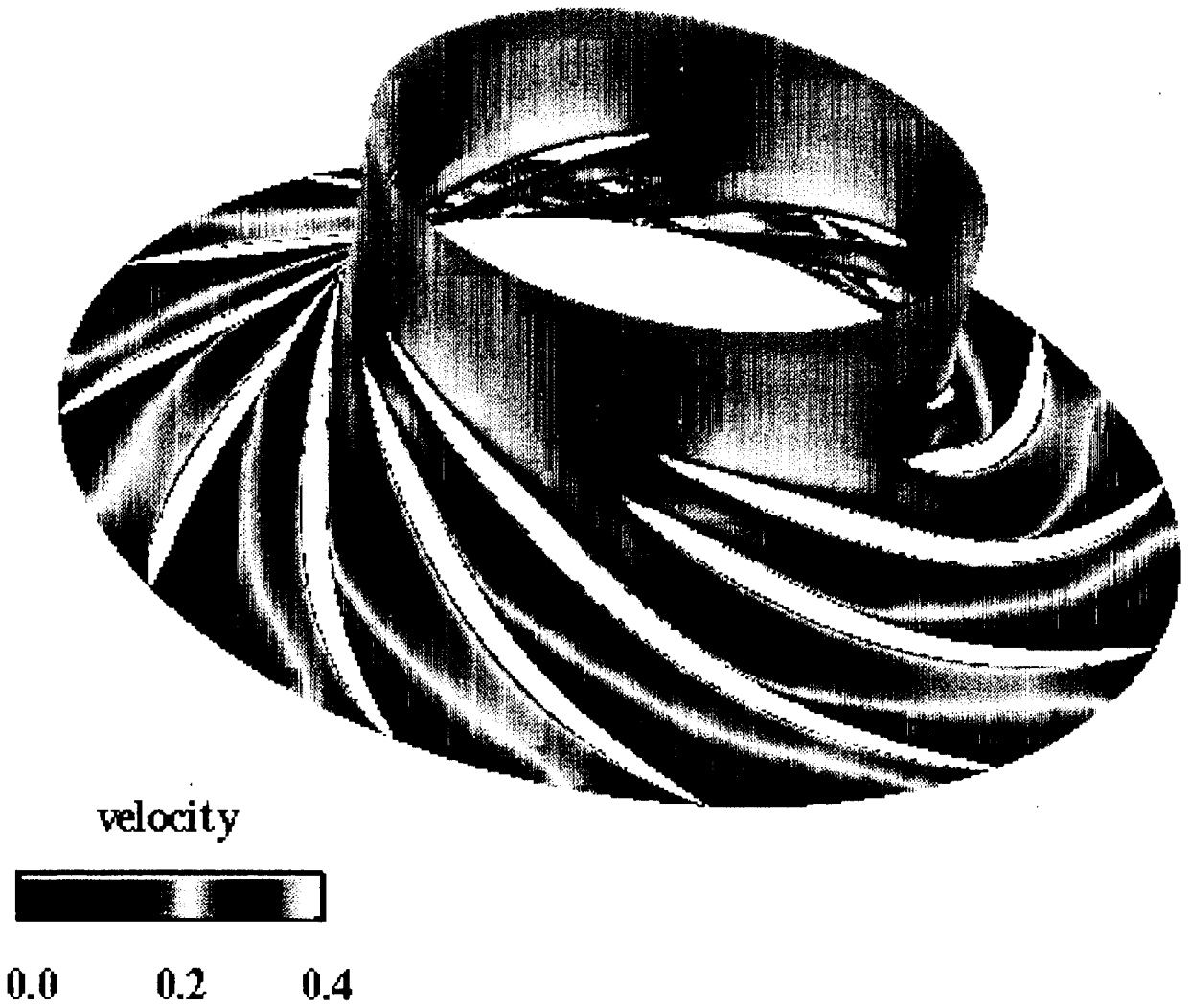

Figure 19. Optimized Impeller with "Longer" Splitter: Velocity Magnitude at Mid-Span.

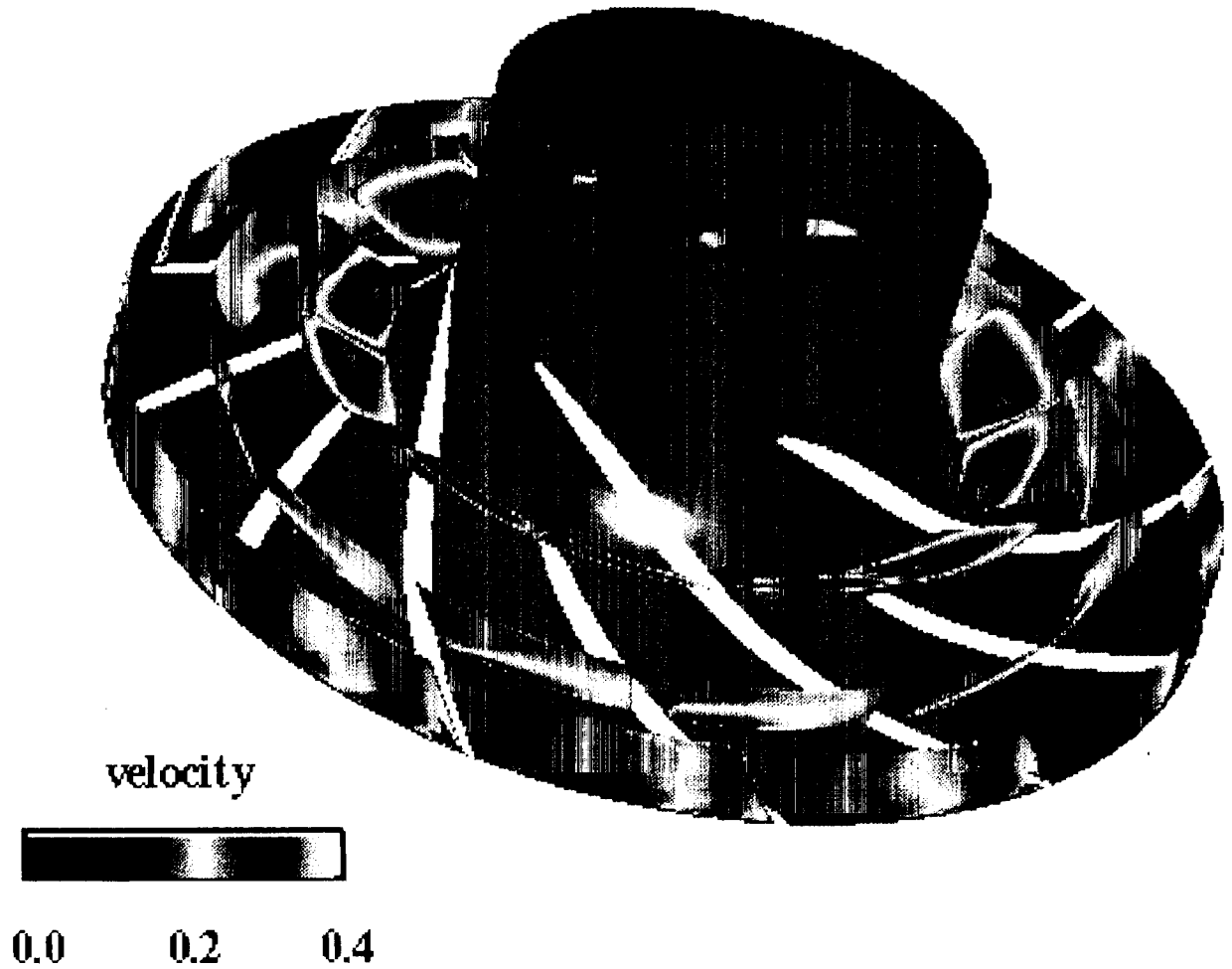

Figure 20. Baseline Impeller: Velocity Magnitude at Three Streamwise Locations.

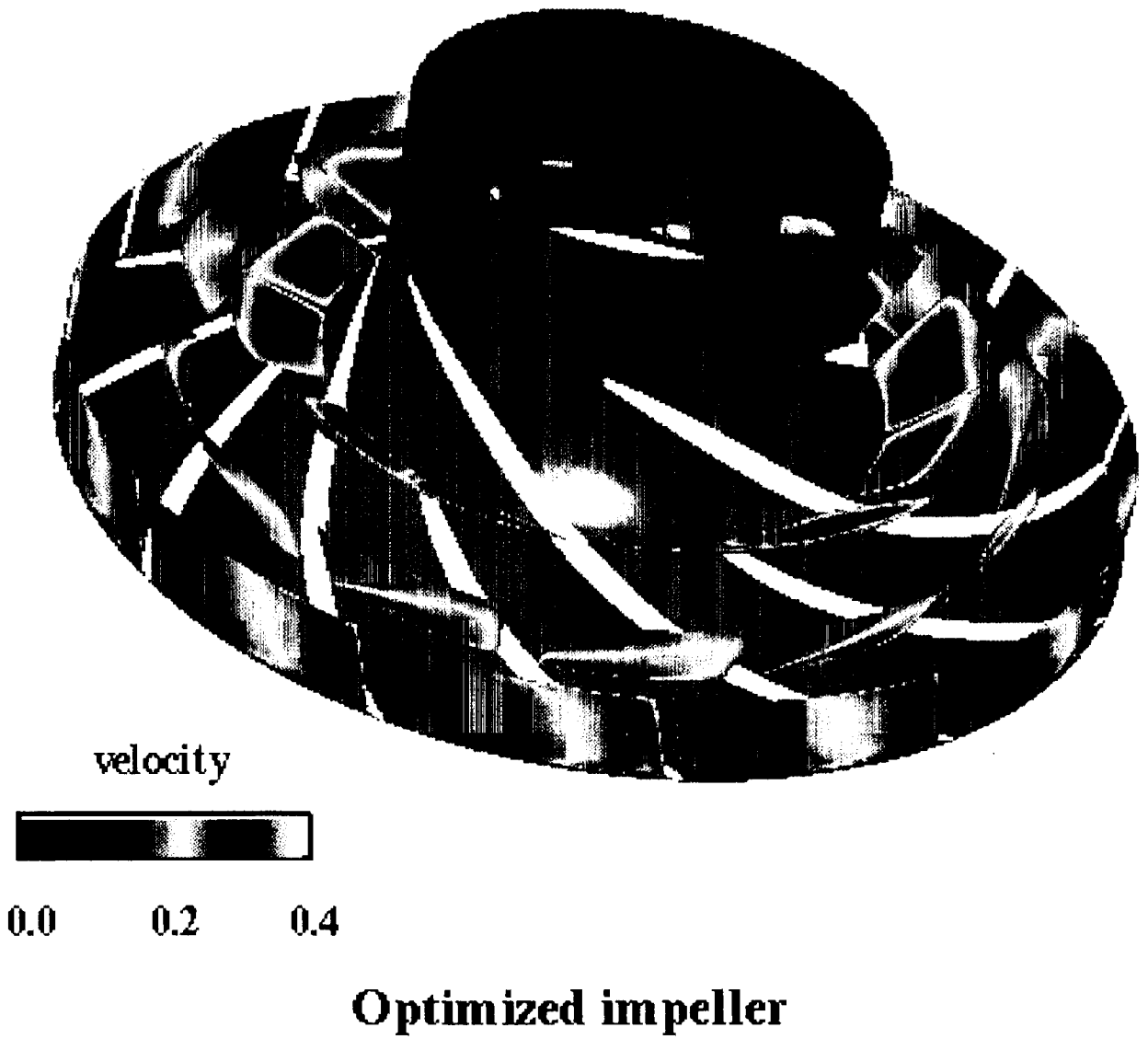

Figure 21. Optimized Impeller: Velocity Magnitude at Three Streamwise Locations.

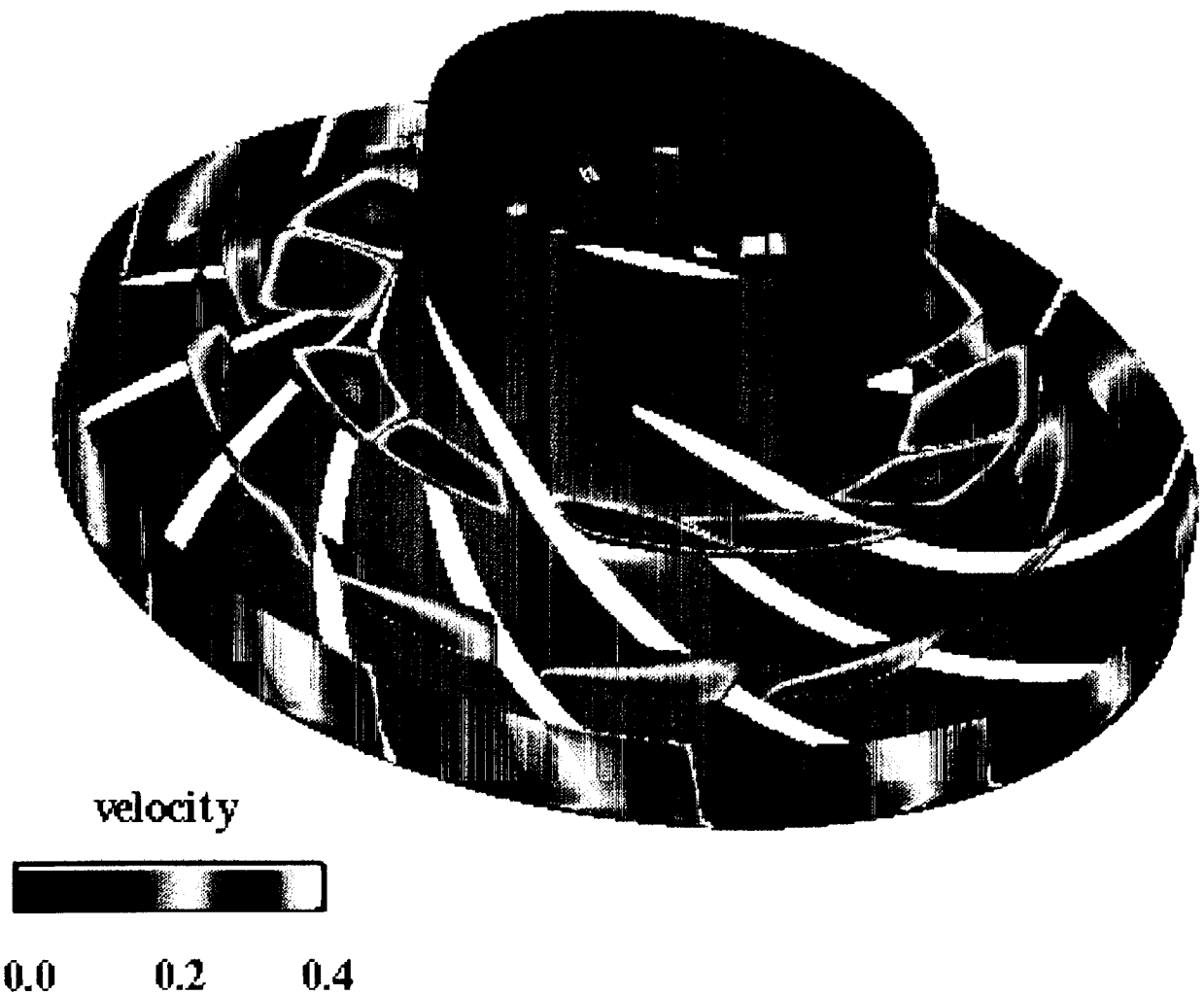

Figure 22. Optimized Impeller with "Long" Splitter: Velocity Magnitude at Three Streamwise Locations.

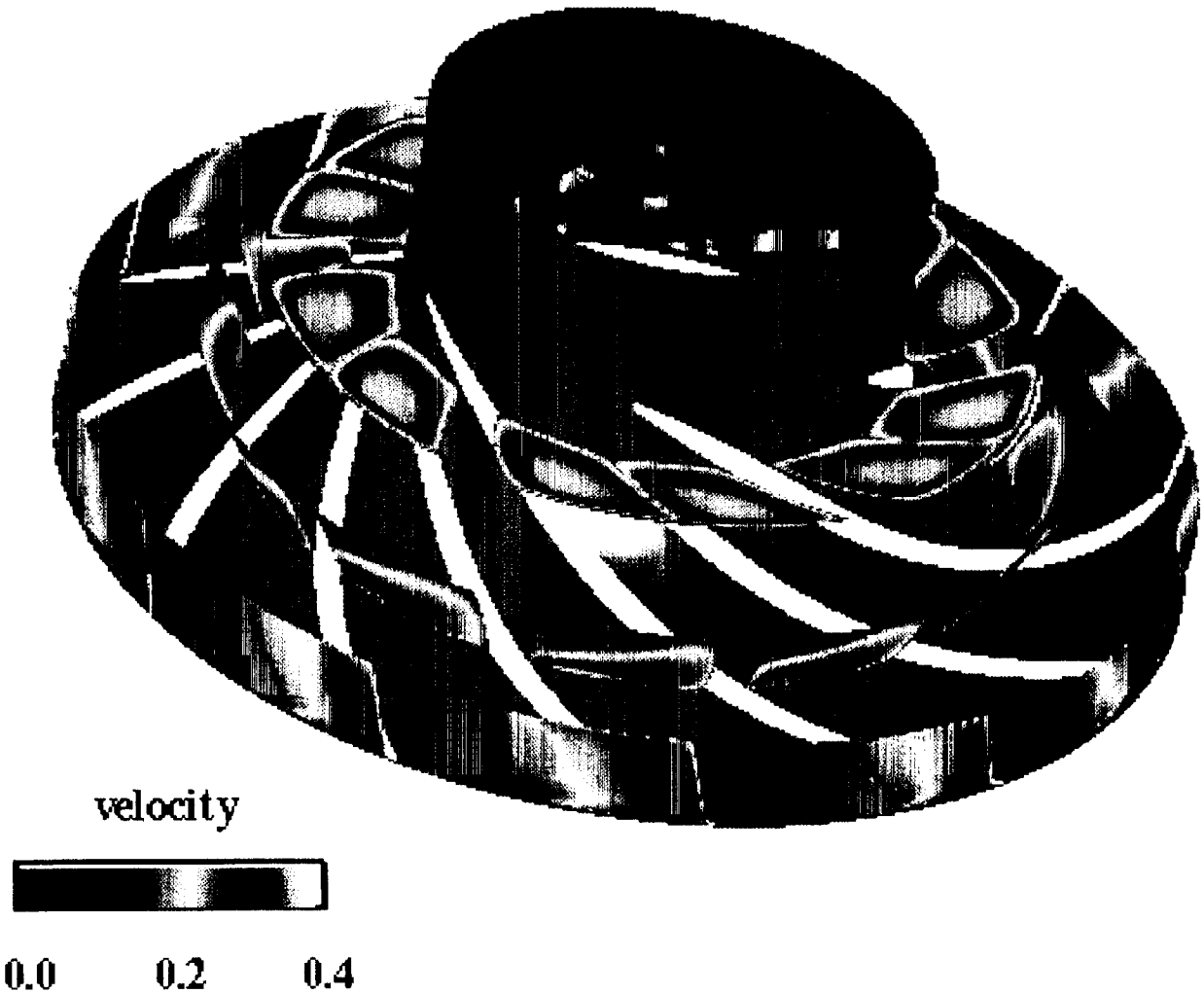

Figure 23. Optimized Impeller with "Longer" Splitter: Velocity Magnitude at Three Streamwise Locations.

Figure 24. SSME HPFTP Impeller.

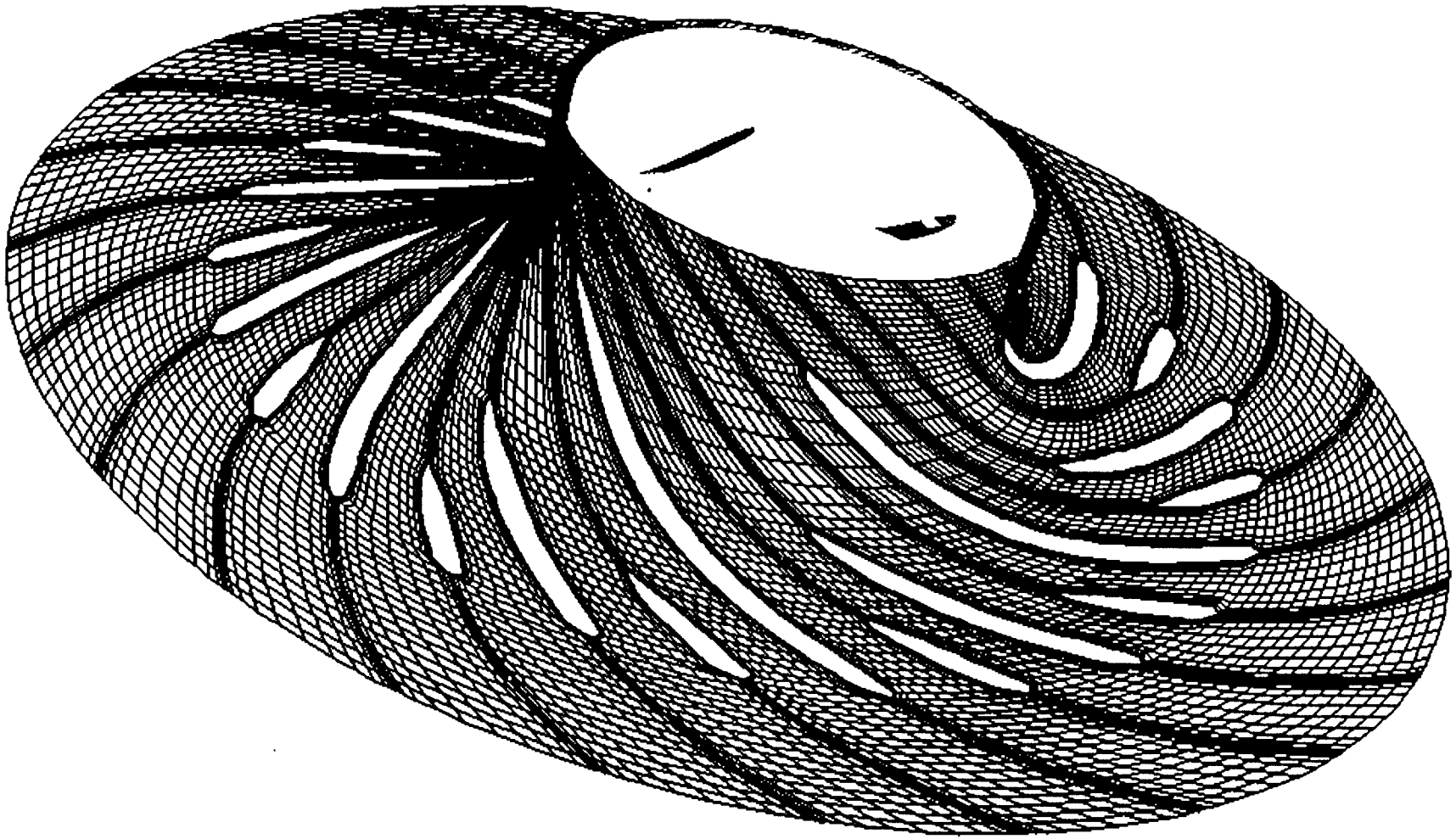

Figure 25. SSME Impeller Grid at Mid-Span.

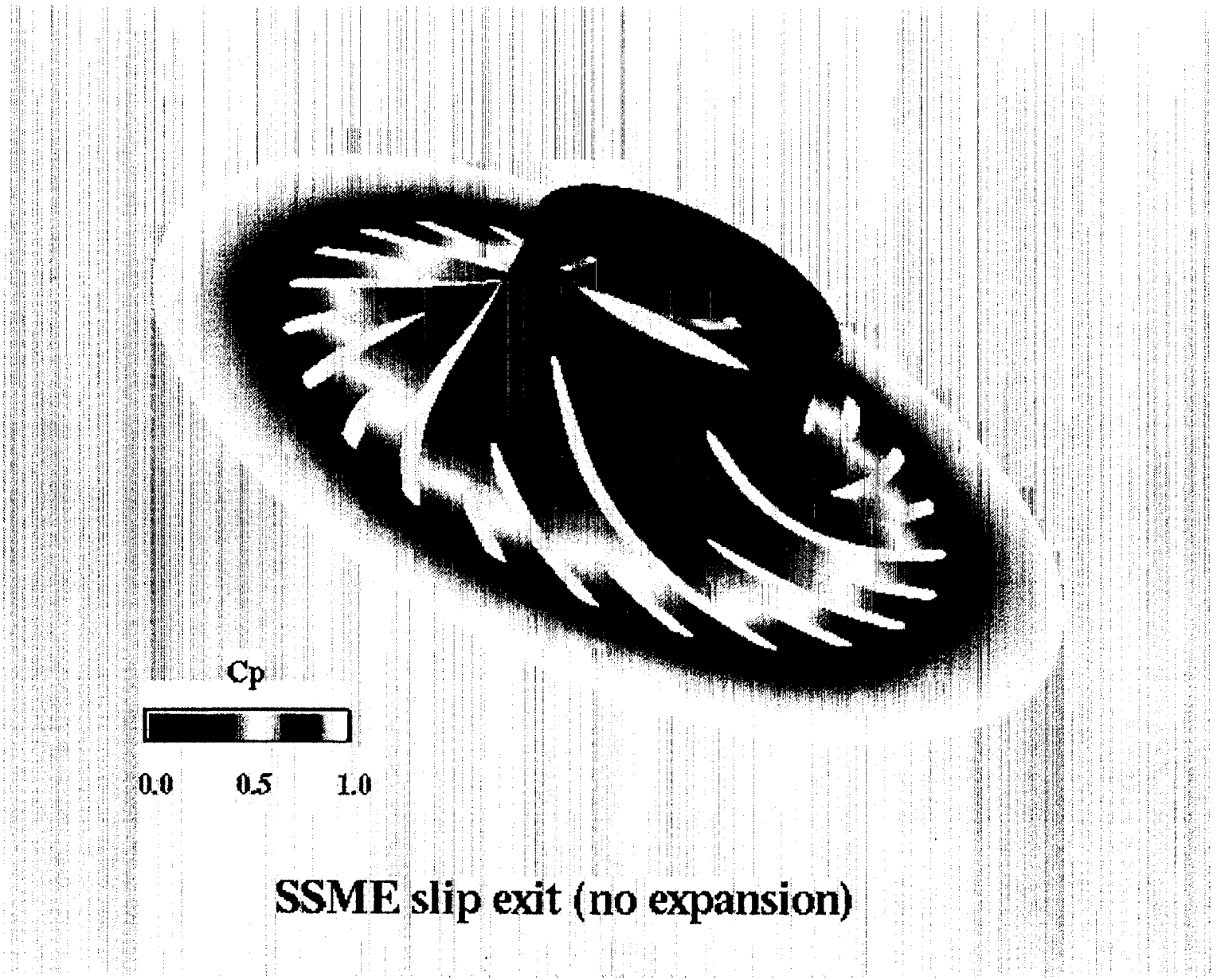

Figure 26. SSME Impeller without Expansion: Pressure Coefficient at Mid-Span.

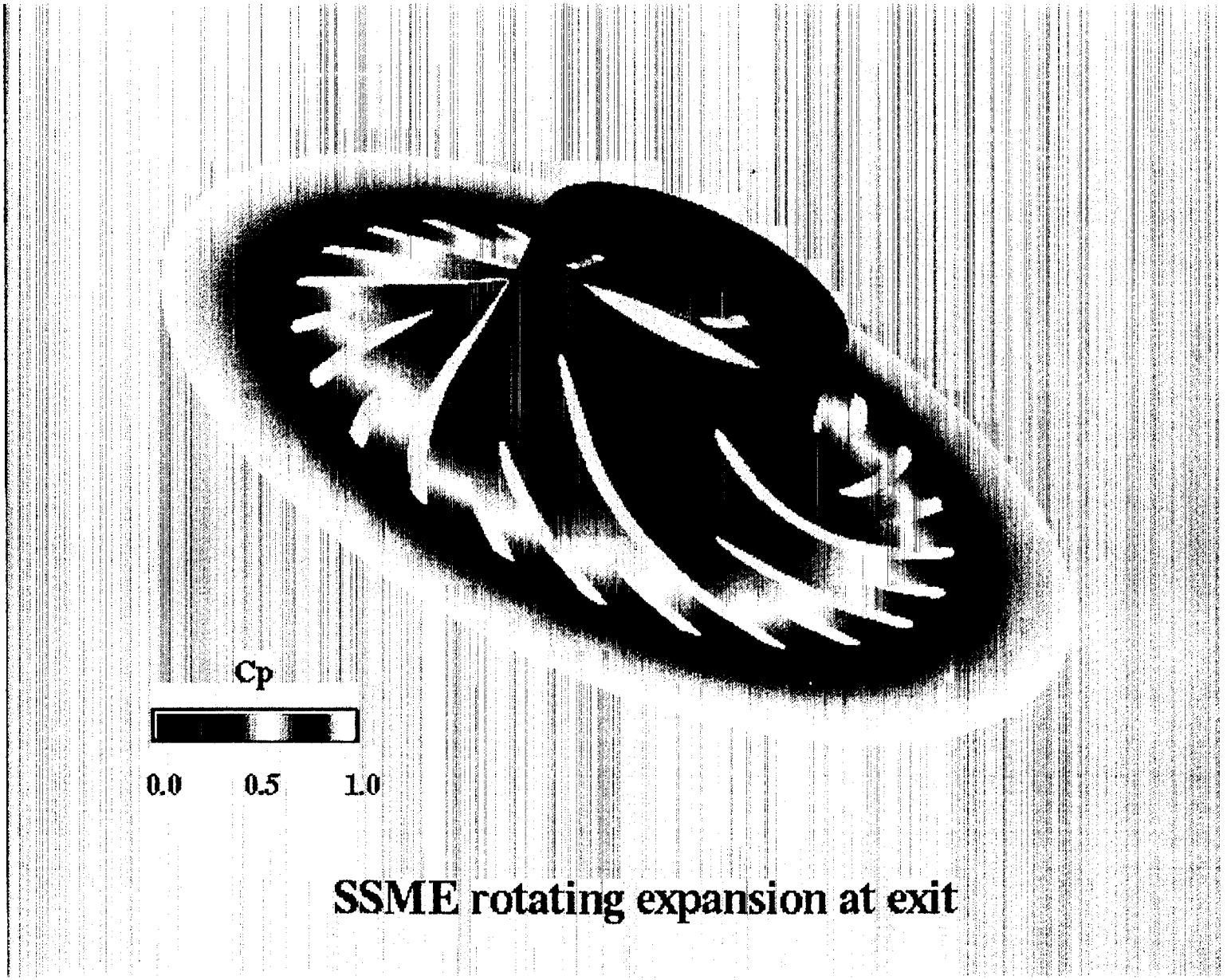

Figure 27. SSME Impeller with Rotating Expansion: Pressure Coefficient at Mid-Span.

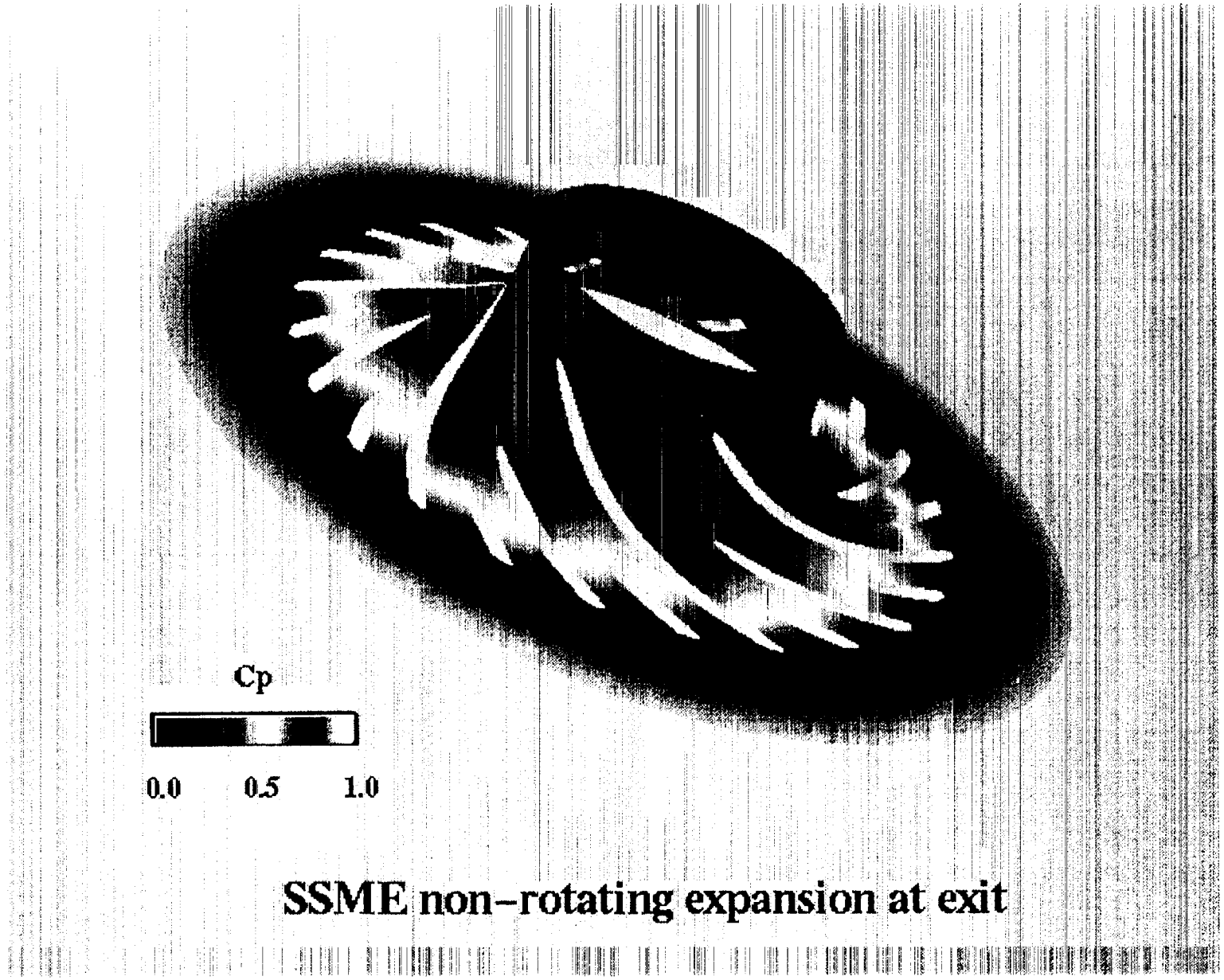

Figure 28. SSME Impeller with Non-Rotating Expansion: Pressure Coefficient at Mid-Span.

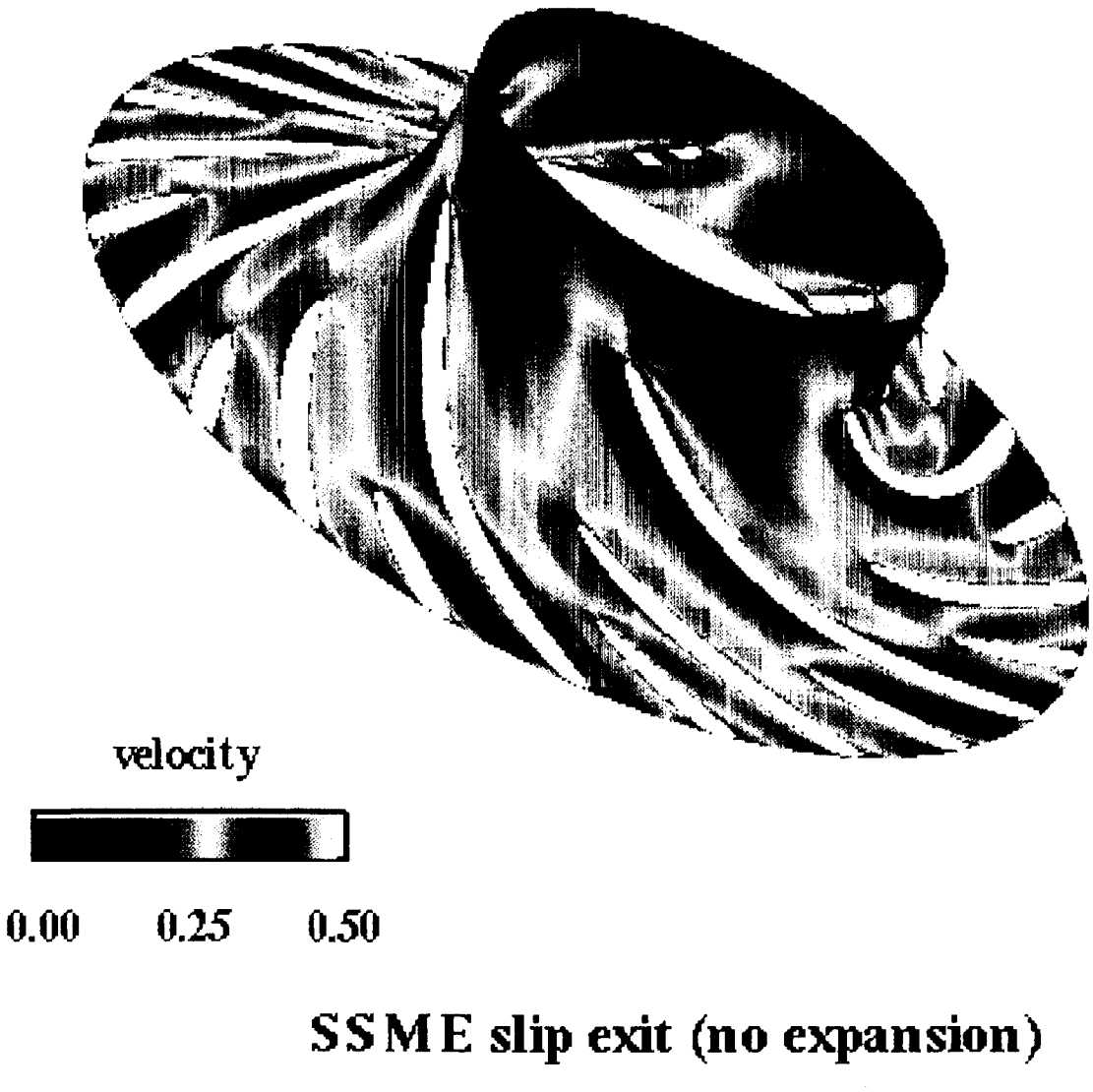

Figure 29. SSME Impeller without Expansion: Velocity Magnitude at Mid-Span.

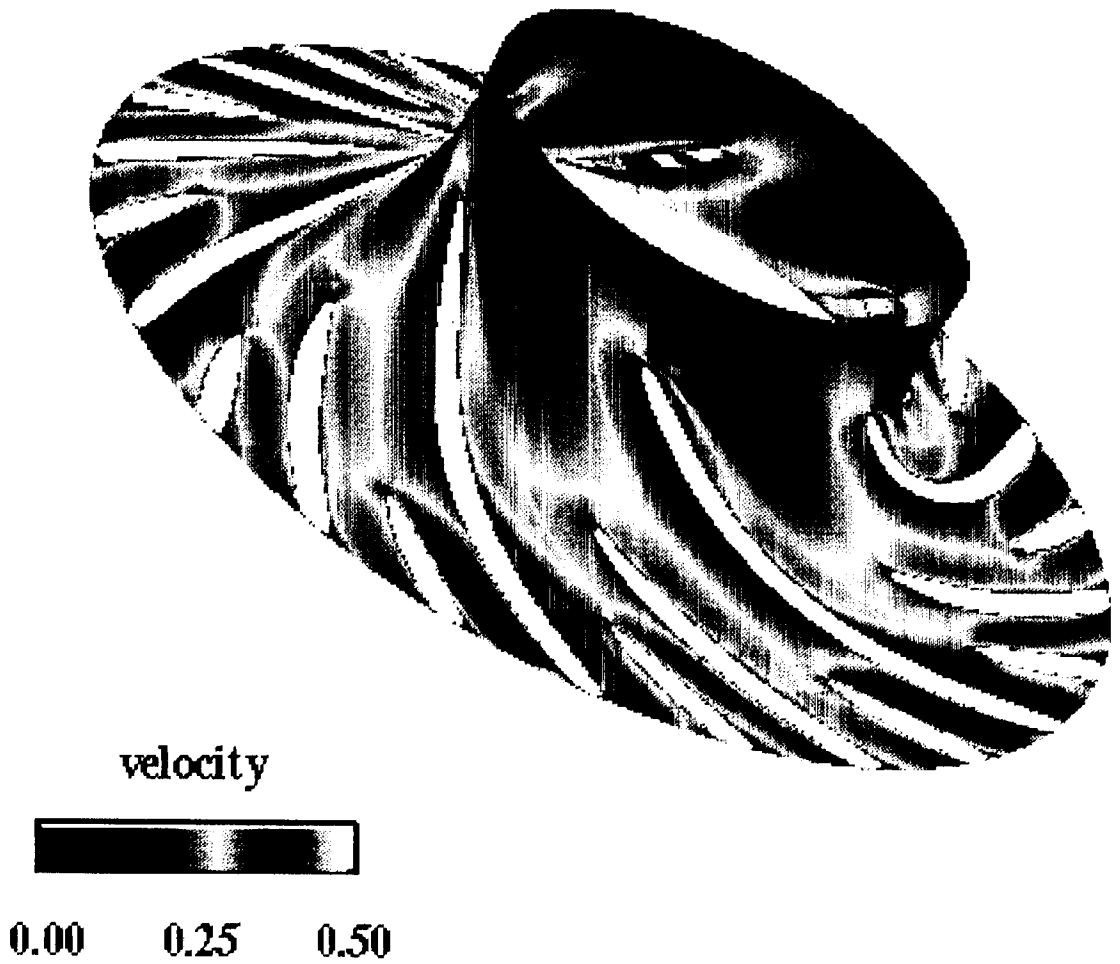

Figure 30. SSME Impeller with Rotating Expansion: Velocity Magnitude at Mid-Span.

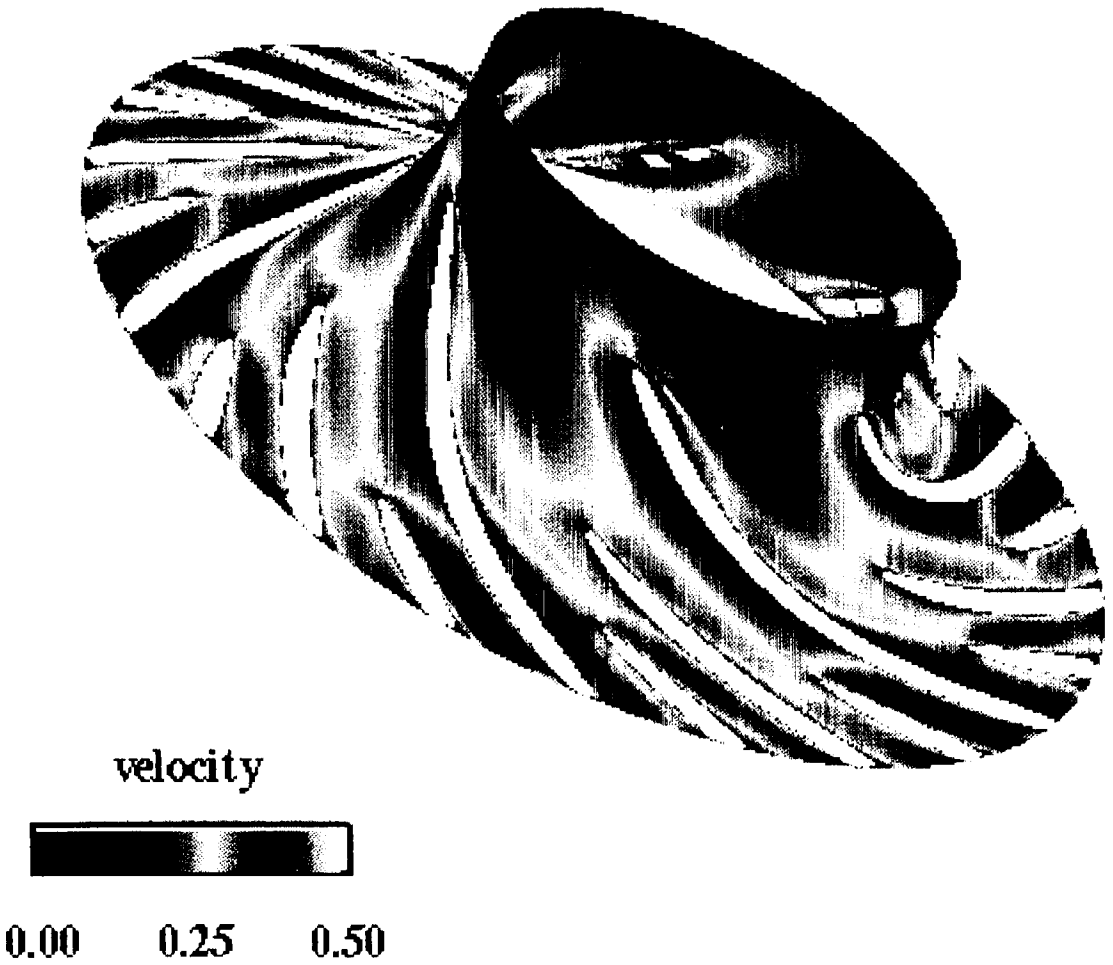

Figure 31. SSME Impeller with Non-Rotating Expansion: Velocity Magnitude at Mid-Span.

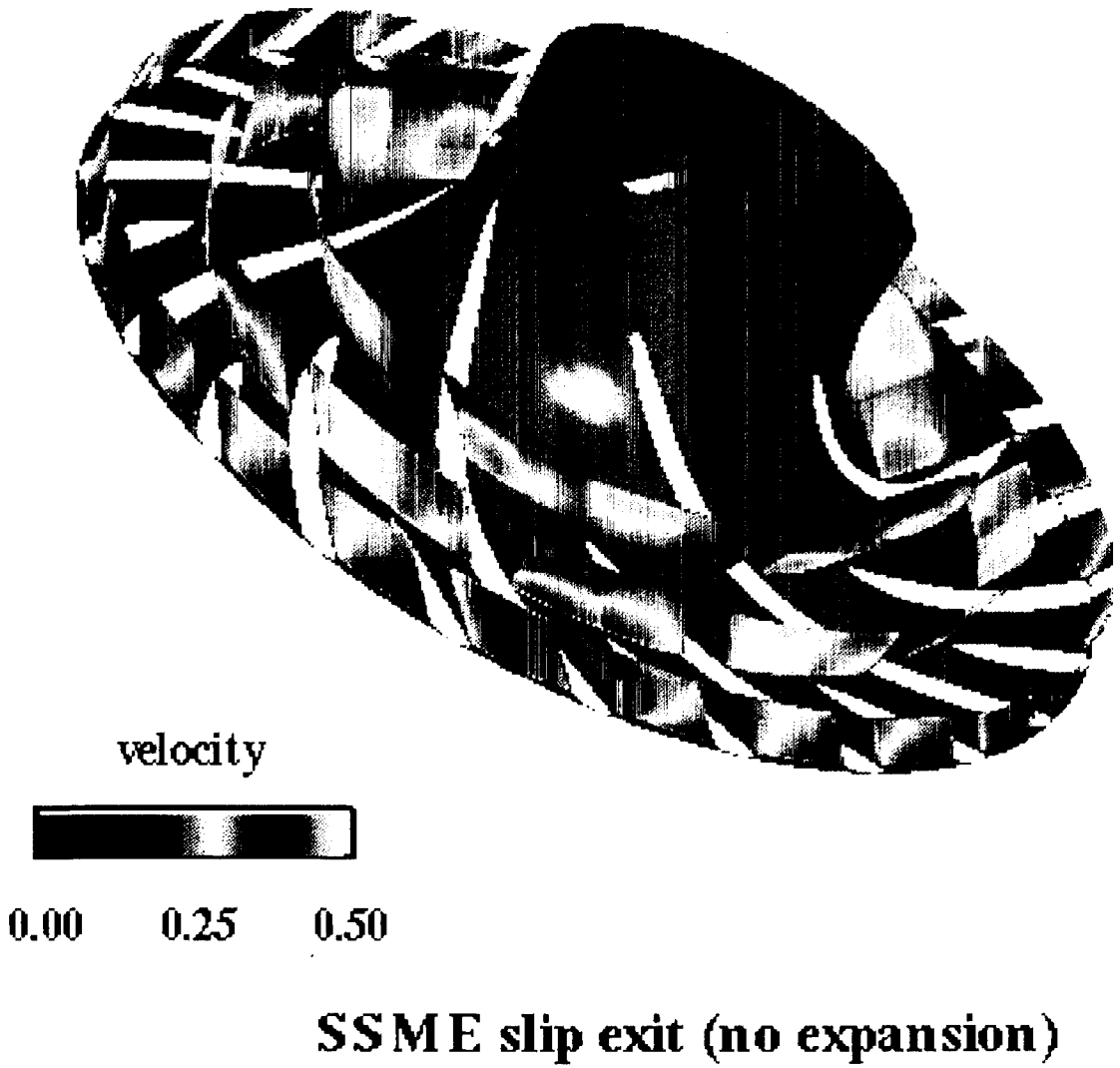

Figure 32. SSME Impeller without Expansion: Velocity Magnitude at Three Streamwise Locations.

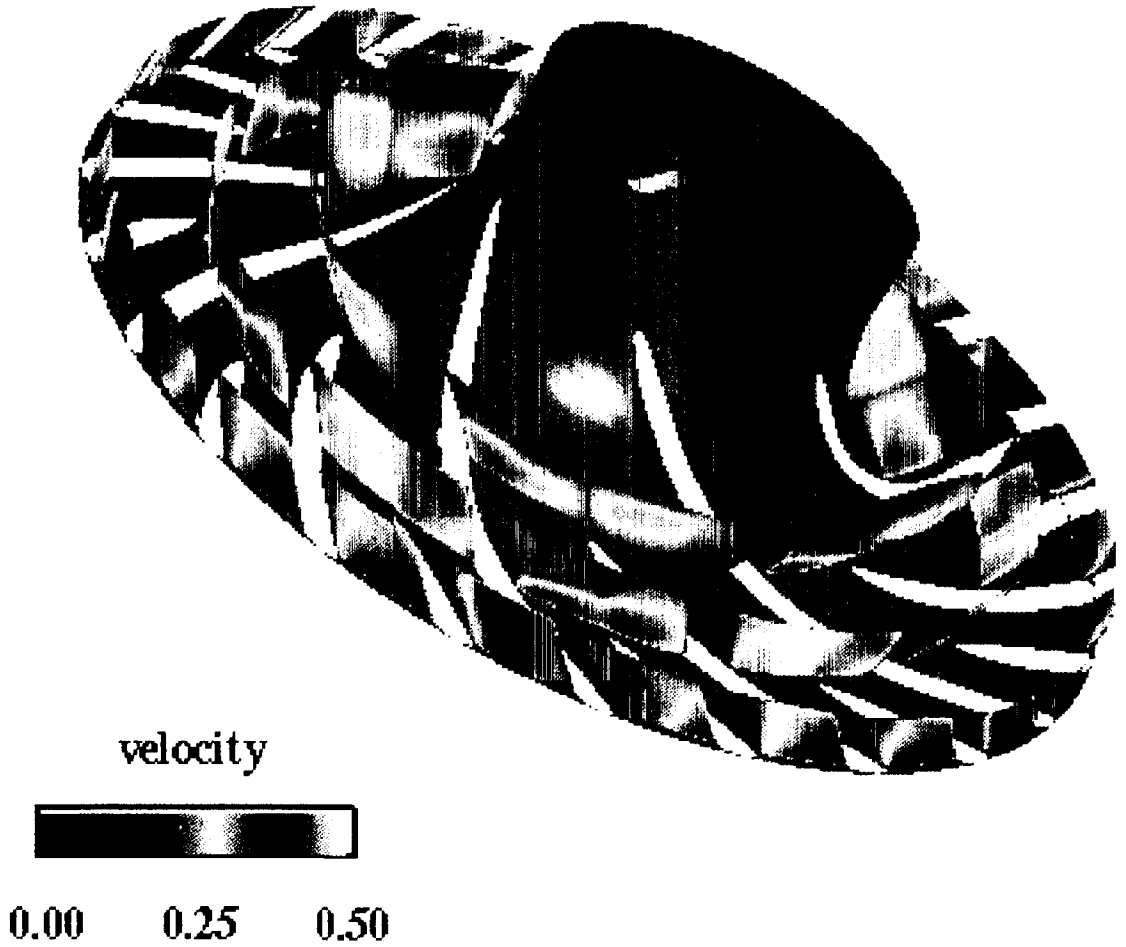

Figure 33. SSME Impeller with Rotating Expansion: Velocity Magnitude at Three Streamwise Locations.

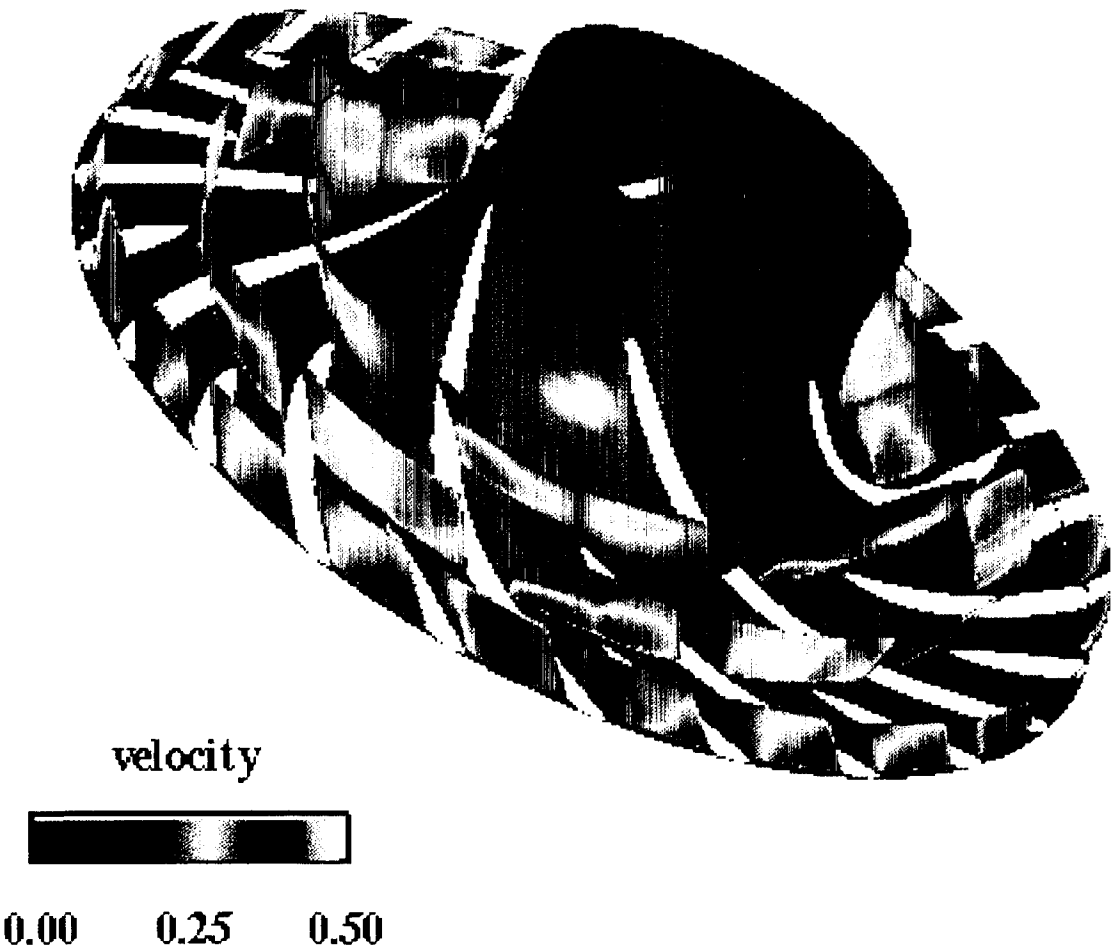

Figure 34. SSME Impeller with Non-Rotating Expansion: Velocity Magnitude at Three Streamwise Locations.

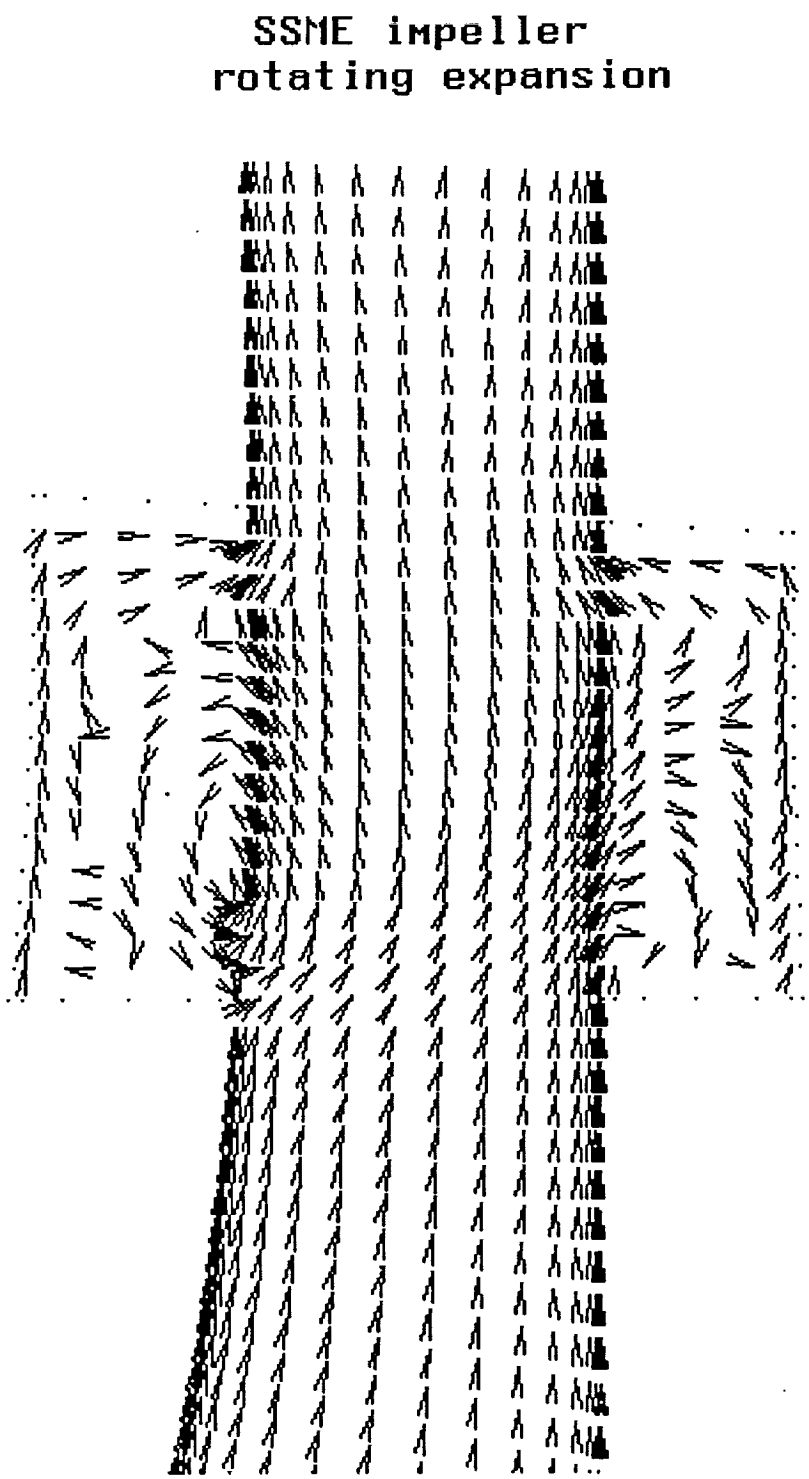

Figure 35. SSME Impeller with Rotating Expansion: Velocity Vectors in a Meridional Plane.

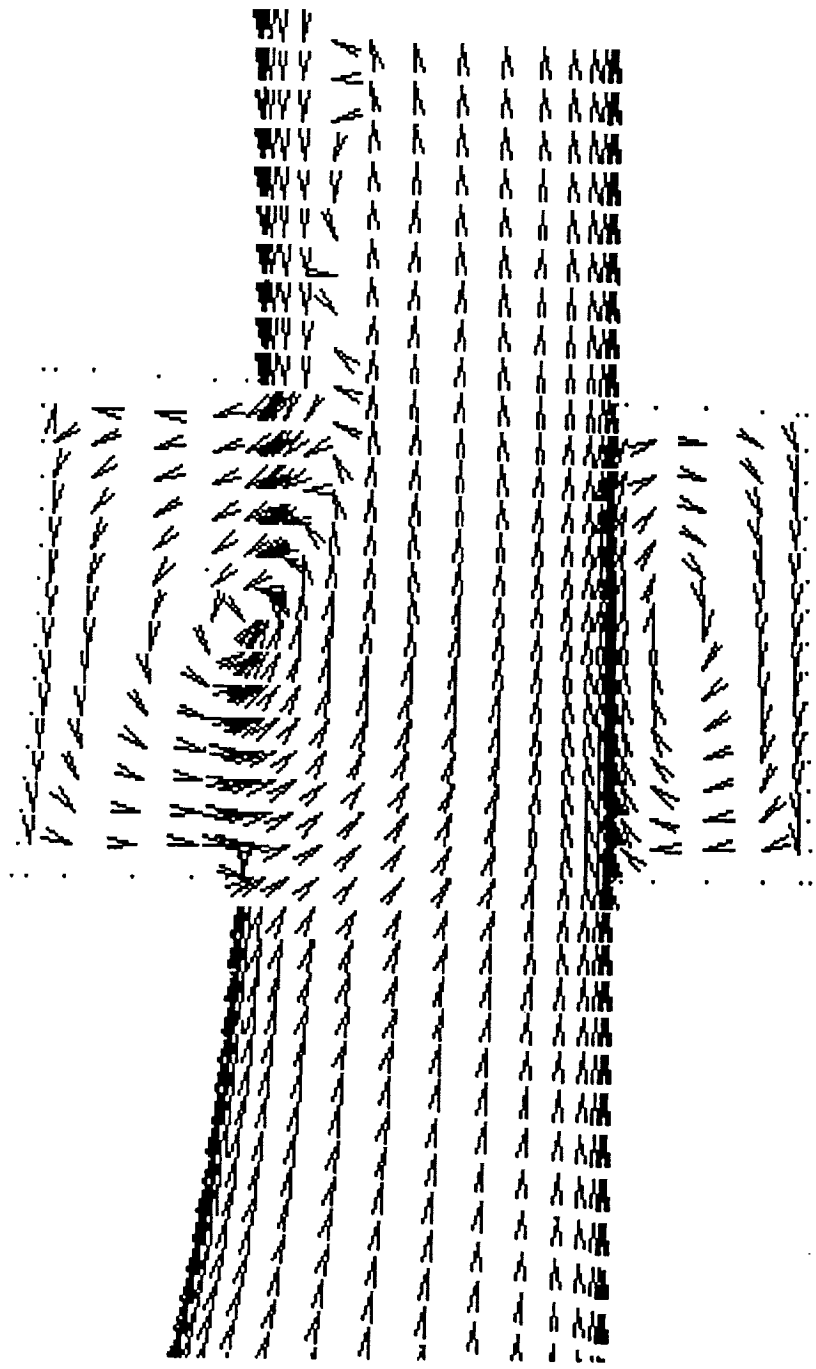

Figure 36. SSME Impeller with Non-Rotating Expansion: Velocity Vectors in a Meridional Plane.

NASA
National Aeronautics and Space Administration

Report Documentation Page

1. Report No.	2. Government Accession No.	3. Recipient's Catalog No.

4. Title and Subtitle

CFD Analysis for Advanced Pump Design

5. Report Date
April 1994

6. Performing Organization Code

7. Author(s)

F.J. de Jong, S-K. Choi and T.R. Govindan

8. Performing Organization Report No.
R94-9081-F

10. Work Unit No.

9. Performing Organization Name and Address

Scientific Research Associates, Inc.
50 Nye Road, P.O. Box 1058
Glastonbury, CT 06033-6058

11. Contract or Grant No.
NAS8-38866

13. Type of Report and Period Covered
Final Jan. 31, 1991 to Jan. 31, 1994

12. Sponsoring Agency Name and Address

National Aeronautics and Space Administration
George C. Marshall Space Flight Center
Hunsvillle, AL 35812

14. Sponsoring Agency Code

15. Supplementary Notes

16. Abstract

As one of the activities of the NASA/MSFC Pump Stage Technology Team, the present effort was focused on using CFD in the design and analysis of high performance rocket engine pumps. Under this effort, a three-dimensional Navier-Stokes code was used for various inducer and impeller flow field calculations. An existing algebraic grid generation procedure was extended to allow for nonzero blade thickness, splitter blades, and hub/shroud cavities upstream or downstream of the (main) blades, resulting in a fast, robust inducer/impeller geometry/grid generation package. Problems associated with running a compressible flow code to simulate an incompressible flow were resolved; related aspects of the numerical algorithm (viz., the matrix preconditioning, the artificial dissipation, and the treatment of low Mach number flows) were addressed. As shown by the calculations performed under the present effort, the resulting code, in conjunction with the grid generation package, is an effective tool for the rapid solution of three-dimensional viscous inducer and impeller flows.

17. Key Words (Suggested by Author(s))	18. Distribution Statement
Rocket Engine, Pump, Inducer, Impeller, Viscous Flow, Navier-Stokes Code, Computational Fluid Dynamics	Unclassified - Unlimited

19. Security Classif. (of this report)	20. Security Classif. (of this page)	21. No. of pages	22. Price
Unclassified	Unclassified	55	

NASA FORM 1626 OCT 86